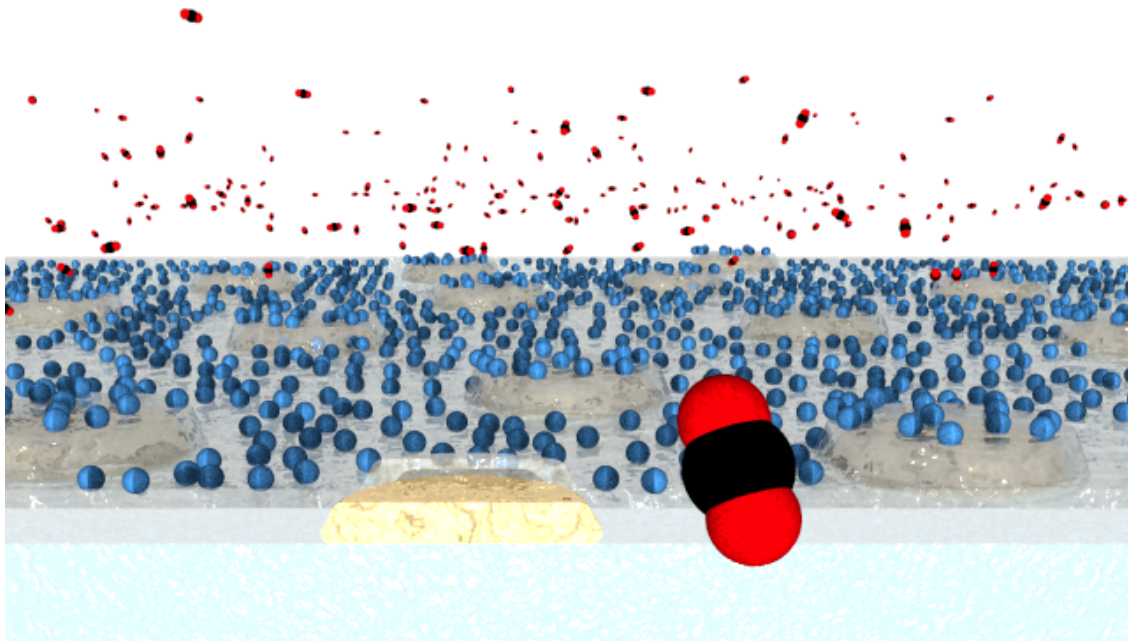




CHALMERS
UNIVERSITY OF TECHNOLOGY



Exploring Colloidal Silica Nanoparticles for Carbon Dioxide Capture and Storage

Optical measurements of CO₂ adsorption by Indirect Nano-
plasmonic Sensing

Master's thesis in Applied Physics

SARA NILSSON

MASTER'S THESIS 2016

Exploring Colloidal Silica Nanoparticles for Carbon Dioxide Capture and Storage

Optical measurements of CO₂ adsorption by Indirect Nanoplasmonic
Sensing

SARA NILSSON



CHALMERS
UNIVERSITY OF TECHNOLOGY

Department of Physics
Division of Chemical Physics
CHALMERS UNIVERSITY OF TECHNOLOGY
Gothenburg, Sweden 2016

Exploring Colloidal Silica Nanoparticles for Carbon Dioxide Capture and Storage
Optical measurements of CO₂ adsorption by Indirect Nanoplasmonic Sensing
SARA NILSSON

© SARA NILSSON, 2016.

Supervisor: Ferry A. A. Nugroho, Department of Physics
Examiner: Christoph Langhammer, Department of Physics

Master's Thesis 2016
Department of Physics
Division of Chemical Physics
Chalmers University of Technology
SE-412 96 Gothenburg
Telephone +46 31 772 1000

Cover: an illustration of the LSPR sensor surface covered with silica nanoparticles exposed to CO₂ in gas phase.

Typeset in L^AT_EX
Printed by Chalmers Reproservice
Gothenburg, Sweden 2016

Exploring colloidal Silica Nanoparticles for Carbon dioxide Capture and Storage
Optical measurements of CO₂ adsorption by Indirect Nanoplasmonic Sensing

SARA NILSSON

Department of Physics

Chalmers University of Technology

Abstract

Reducing the emissions of carbon dioxide is critical to prevent climate change. Carbon dioxide Capture and Storage (CCS) provides one step in that direction. Mesoporous materials, such as silica, are studied as sorption materials for CCS to decrease the energy demand of regeneration compared to the more frequently used liquid amines. In the search for the optimal sorption material, the isosteric heat of adsorption, Q_{st} , of CO₂ is a key factor to consider. In this project the CO₂ adsorption ability of colloidal silica nanoparticles (NP) provided by AkzoNobel PPC AB was measured optically using Indirect Nanoplasmonic Sensing (INPS). INPS relies on Localized Surface Plasmon Resonance (LSPR), which is highly sensitive to the refractive index of the surrounding medium. Thus, it constitutes a suitable tool for detecting gas adsorption on solid surfaces. Specifically, INPS provides an effective way of studying CO₂ adsorption without influencing the sample and without calibration. Colloidal silica nanoparticles of two sizes were studied, along with two types of amine functionalizations. A reproducible method for depositing the silica nanoparticles on the INPS sensor surface was developed. It was established that the silica particles indeed adsorb CO₂ and a larger LSPR response was obtained for the smaller particles due to their larger specific surface area. The estimated isosteric heat of adsorption agreed well with literature. The average value for bare silica particles was 19.9 kJ/mol and for amine functionalized NPs the average isosteric heat was slightly lower, namely 14.6 kJ/mol.

Keywords: Nanoplasmonics, CCS, colloidal silica, LSPR, INPS, sensing, isosteric heat of adsorption, HCL.

Acknowledgements

First of all, I want to thank Christoph Langhammer for giving me the opportunity of doing this truly interesting and challenging thesis work, for taking time to answer my questions and by his supervision leading the project forward. I also want to thank my supervisor Ferry Nugroho, who taught me the cleanroom fabrication and always had time to help me or discuss my ideas. I want to thank David Albinsson for many fruitful discussions and for answering my stupid questions. Thanks to the entire group of Chemical Physics for supporting such a friendly and openhearted environment and for providing many enjoyable fika times.

Thanks to Michael Persson at AkzoNobel PPC AB for making this project possible by providing the silica samples and the silica expertise knowledge.

A great thanks is also sent to my friends for all hours of discussion during the years of studying together. Last but not least, I want to thank my family for supporting me through all these years of hard work and for always believing in me.

Sara Nilsson, Gothenburg, March 2016

Contents

List of Figures	xiii
List of Tables	xix
1 Introduction	1
2 Carbon dioxide Capture and Storage	3
2.1 The principle of Carbon dioxide Capture and Storage	3
2.2 Amine functionalized silica for CCS	4
3 Theoretical background	7
3.1 Charged particles in solution	7
3.1.1 Electrical double layer	7
3.1.2 Colloidal silica	9
3.2 Calculating the isosteric heat of adsorption	9
3.2.1 Chemisorption and physisorption	10
3.2.2 Langmuir adsorption model	10
3.2.3 Isosteric heat by the Gibbs-Helmholtz equation	10
3.3 Nanoplasmonics	11
3.3.1 Harmonic model of electrons in metals	11
3.3.2 Quasi-electrostatic approximation	12
3.3.3 Localized Surface Plasmon Resonance sensing	13
3.3.4 Indirect Nanoplasmonic Sensing	15
4 Nanofabrication	17
4.1 Plasmonic sensors produced by Hole-Mask Colloidal Lithography	17
4.2 Chemical vapor deposition of dielectric spacer layer	18
4.3 Silica nanoparticle deposition	19
5 Analysis methods	21
5.1 Optical CO ₂ adsorption measurements: X1 setup	21
5.2 Characterization of silica particle layers by scanning electron microscopy	22
5.3 Extinction spectrum measurement	23
6 Result	25
6.1 Investigating background signal from gold nanodiscs, spacer layer and cationic polymer	25

6.1.1	Gold nanodiscs	26
6.1.2	Material choice for dielectric spacer layer	27
6.1.3	Thickness of dielectric spacer layer	28
6.1.4	Cationic polymer	30
6.2	Extinction spectra	31
6.3	CO ₂ adsorption on silica nanoparticles	31
6.3.1	CO ₂ adsorption on silica nanoparticles deposited by procedure 2	32
6.3.2	CO ₂ adsorption on silica nanoparticles deposited by procedure 3	34
6.4	CO ₂ adsorption on silica nanoparticles functionalized by amine groups	36
6.5	Average isosteric heat of adsorption	39
7	Conclusion and outlook	43
A	Appendix 1	I
A.1	170 nm Au nanodiscs	I
A.2	Control measurement of adsorption on polymer	II
A.3	Silica NPs deposited by procedure 1 and 2	II
A.4	Control measurement of silica NPs deposited by procedure 3	III
A.5	Amine functionalized silica NPs deposited by procedure 2	IV
B	Appendix 2	V
B.1	Langmuir model fit parameters	V
B.2	Isosteric heats from all measurements	IX
C	Appendix 3	XI
C.1	7 nm silica NPs imaged at 70 degree angle	XI
C.2	20 nm silica NPs on Si ₃ N ₄	XI

Acronyms

- APTS** (3-aminopropyl)triethoxysilane. 4
- CCS** Carbon dioxide Capture and Storage. 3
- EDA** N-[3- (trimethoxysilyl)propyl]ethylenediamine. 4
- FTIR** Fourier Transform Infrared. 5
- HCL** Hole-Mask Colloidal Lithography. 17
- INPS** Indirect Nanoplasmonic Sensing. 15
- LSPR** Localized Surface Plasmon Resonance. 13
- MEA** monoethanolamine. 3
- MSP** Mesoporous Spherical-Silica Particles. 4
- NP** nanoparticle. 12
- PE-CVD** Plasma Enhanced Chemical Vapor Deposition. 18
- PEI** polyethyleneimine. 4, 5
- PMMA** poly(methyl methacrylate). 17
- PS** polystyrene. 18
- QCM** Quartz Crystal Microbalance. 27
- RI** refractive index. 14
- SEM** Scanning Electron Microscope. 21–23

List of Figures

2.1	Common molecules used for functionalization of porous silica support structures to enhance CO ₂ adsorption. (a) APTS ((3-aminopropyl) triethoxysilane) and (b) PEI (polyethyleneimine).	4
2.2	To the left, a surface functionalized by alkyl chains terminated by amine groups. To the right, two different types of chemisorbed CO ₂ that may form depending on the amine loading and heterogeneity of the loading. Shown above is the alkylammonium-carbamate ion pair and below the surface-bound carbamate.	5
3.1	Schematic figure explaining the model of an electrical double layer around a charged particle in solution. The model is a combination of the Helmholtz counterion layer, also known as Stern layer, and the Gouy-Chapman model of a diffusive layer.	8
3.2	Excited localized surface plasmon. An externally applied field, with wavelength $\lambda \gg r$, where r is the nanosphere radius, can excite the free electron cloud of the particle and make it oscillate. Thus, the nanoparticle turns into a time-dependent dipole, which is called a localized surface plasmon, because it is confined by the geometry of the sphere.	13
3.3	Schematic figure illustrating the principle of LSPR sensing. Receptors are immobilized on the nanoparticles and when analytes bind to these the LSPR extinction peak red-shifts due to the increase in dielectric constant of the surrounding medium. The binding event is detected by measuring the extinction spectrum change.	14
3.4	Schematic figure illustrating the principle of INPS sensing. INPS is a LSPR technique where the plasmonic particles (here nanodiscs) are covered with a dielectric spacer layer, both to protect them from any interaction with the material of interest and to provided tailored surface properties. Gas adsorbed within the sensing volume of one nanodisc yields a red-shift in plasmonic resonance due to the change in RI.	16

4.1	Schematic figure of the fabrication steps in Hole-Mask Colloidal Lithography (HCL). First a PMMA layer is spin-coated on the substrate and PS beads are self-assembled on top. A 15 nm Cr thin film is evaporated on the sample, in which holes are made by tape-stripping of the PS beads. Holes in the PMMA are etched by oxygen plasma and a 20 nm Au thin film is evaporated over the sample, which finally is lifted off by dipping into acetone, producing Au nanodiscs.	18
5.1	Schematic sketch of the measurement setup X1 used for CO ₂ adsorption measurements. The sensor chip was mounted in the middle of the reactor, white light irradiated the sample, transmitted light was collected by the optical fiber and analyzed by the spectrometer. The temperature was controlled by a thermocouple.	22
6.1	The surface of an INPS chip imaged by SEM, (a) from the top and (b) at 70° angle. The gold nanodiscs fabricated by HCL are evenly distributed over the surface. The edges of the discs look smooth due to the Si ₃ N ₄ spacer layer.	26
6.2	LSPR wavelength shift of bare gold nanodiscs. CO ₂ was flushed through the reactor during intervals of 7.5 minutes, at partial pressures 25, 50, 75 and 100% of 1 atm (grey fields) at each temperature; 338 K (blue), 318 K (orange) and 298 K (yellow). In between the CO ₂ intervals, the system was flushed with pure Ar for equally long time, to desorb the CO ₂	27
6.3	LSPR wavelength shift of an INPS chip coated by dielectric spacer layer of (a) 10 nm SiO ₂ and (b) 10 nm Si ₃ N ₄ . CO ₂ was flushed through the reactor for 5 minutes each time, at partial pressures 25, 50, 75 and 100% of 1 atm (grey fields) at each temperature; 358 K (blue), 338 K (orange), 318 K (yellow) and 298 K (purple). In between the system was flushed with pure Ar for equally long time, to desorb the CO ₂	28
6.4	LSPR wavelength shift of an INPS chip coated by dielectric spacer layer of (a) 5 nm Si ₃ N ₄ , (b) 10 nm Si ₃ N ₄ and (c) 15 nm Si ₃ N ₄ . CO ₂ was flushed through the reactor for 7.5 minutes each time, at partial pressures 25, 50, 75 and 100% of 1 atm (grey fields) at each temperature; 358 K (blue), 338 K (orange), 318 K (yellow) and 298 K (purple).	29
6.5	LSPR shift $\Delta\lambda$ of cationic polymer on an INPS chip. CO ₂ was flushed through the reactor during intervals of 7.5 minutes, at partial pressures 25, 50, 75 and 100% of 1 atm (grey fields) at each temperature; 358 K (blue), 338 K (orange), 318 K (yellow) and 298 K (purple).	30
6.6	Extinction spectrum of (a) a bare INPS chip and (b) an INPS chip coated with 1 up to 8 depositions of 1wt% 20 nm silica particles according to procedure 2.	31

6.7	The LSPR peak wavelength as a function of the number of silica depositions according to procedure 2 but using the lower concentration of 1wt% instead. The peak red-shifts linearly when adding more silica. The dashed line is a fit to the data excluding the peak after the fourth deposition.	32
6.8	LSPR shift for CO ₂ adsorption on a sensor with (a) 7 nm and (b) 20 nm silica particles, both deposited by procedure 2. CO ₂ exposure of 7.5 minutes each time, at partial pressures 25, 50, 75 and 100% of 1 atm (grey fields) at each temperature; 358 K (blue), 338 K (orange), 318 K (yellow) and 298 K (purple). Note the unexpected relation between $\Delta\lambda$ for the two particles sizes.	33
6.9	LSPR shift for CO ₂ adsorption on a sensor with (a) 7 nm and (b) 20 nm silica particles, both deposited by procedure 3. As expected, the smaller particles yield a larger $\Delta\lambda$. CO ₂ exposure of 7.5 minutes each time, at partial pressures 25, 50, 75 and 100% of 1 atm (grey fields) at each temperature; 358 K (blue), 338 K (orange), 318 K (yellow) and 298 K (purple).	35
6.10	Si surface covered with 7 nm silica particles deposited either by (a) procedure 2, 5 repetitions or (b) procedure 3. Even though the right image is not sharp, one can see that there is a thicker and denser multi-layer compared to slightly more than a monolayer in the left image.	35
6.11	INPS chip with 7 nm silica NPs deposited by procedure 3, (a) from above and (b) at 70° angle. We can see silica NPs on top of the gold nanodiscs, however, the coverage is not at all as high as on a Si surface.	36
6.12	LSPR shift for CO ₂ adsorption on 7 nm silica functionalized by (a) monoamines and (b) triamines, in both cases deposited by procedure 3. CO ₂ exposure of 7.5 minutes each time, at partial pressures 25, 50, 75 and 100% of 1 atm (grey fields) at each temperature; 358 K (blue), 338 K (orange), 318 K (yellow) and 298 K (purple).	37
6.13	Longer CO ₂ adsorption run at 298 K in X1 gas setup. Adsorption measured during 20 hours followed by desorption for 20 hours. It is obvious that the steady state for the adsorption is not yet reach after 20 hours, however, desorption seems to level out at 0.8. The LSPR red-shifts caused by the two different processes are marked as well as the desorption steady state.	38
6.14	The parameters from fitting the data to the Langmuir adsorption model for (a) 7 nm and (b) 20 nm silica NPs, deposited by procedure 3. $\ln(K)$ is plotted as function of T^{-1} , according to the Van't Hoff equation the enthalpic change i.e. the negative isosteric heat, is the slope of the line. The black line is the linear fit.	40

6.15	The average isosteric heat of adsorption for each of the four systems studied, from the left; 7 nm silica NPs with monoamines, with triamines, bare 20 nm silica NPs and bare 7 nm silica NPs. The errorbars are taken as the maximum deviation from the average of measurements. For the 20 nm the average is taken over 5 measurements, for the remaining cases the average is over 3 measurements. The dashed lines are the average isosteric heat of bare silica NPs (the upper line) and silica NPs functionalized with amines (the lower line).	41
A.1	LSPR wavelength shift of an INPS chip with Au discs of diameter (a) 140 nm and (b) 170 nm, covered with silica NPs deposited by procedure 1. There is no significant difference in the LSPR response, the magnitude of the shifts are comparable, and as discussed previously not reliable from procedure 1 or 2. CO ₂ partial pressures 25, 50, 75 and 100% (grey fields) at temperatures 358 K (blue), 338 K (orange), 318 K (yellow) and 298 K (purple).	I
A.2	LSPR wavelength shift of an INPS chip with cationic polymer drop-coated for 2 minutes. CO ₂ partial pressures 25, 50, 75 and 100% (grey fields) at temperatures 358 K (blue), 338 K (orange), 318 K (yellow) and 298 K (purple).	II
A.3	LSPR wavelength shift of an INPS chip with 20 nm silica NPs deposited by (a) procedure 1 and (b) procedure 2. CO ₂ partial pressures 25, 50, 75 and 100% (grey fields) at temperatures 358 K (blue), 338 K (orange), 318 K (yellow) and 298 K (purple).	II
A.4	LSPR wavelength shift of an INPS chip with (a) 7 nm NPs and (b) 20 nm NPs deposited by procedure 3. CO ₂ partial pressures 25, 50, 75 and 100% (grey fields) at temperatures 358 K (blue), 338 K (orange), 318 K (yellow) and 298 K (purple).	III
A.5	LSPR wavelength shift of an INPS chip with (a) monoamine functionalized 7 nm NPs and (b) triamine functionalized, all deposited by procedure 2. CO ₂ partial pressures 25, 50, 75 and 100% (grey fields) at temperatures 358 K (blue), 338 K (orange), 318 K (yellow) and 298 K (purple). Note that in this case, the monoamine has the largest shifts.	IV
A.6	LSPR wavelength shift of an INPS chip with (a) monoamine functionalized 7 nm NPs and (b) triamine functionalized, all deposited by procedure 2. CO ₂ partial pressures 20, 40, 60, 80 and 100% (grey fields) at temperatures 358 K (blue), 348 K (orange), 338 K (yellow), 328 K (purple), 318 K (green), 308 K (light-blue) and 298 K (red). Note that in this case, the triamine has the largest shifts, oppositely to the previous samples. These are not the same samples as above, but from the same batch of INPS chips.	IV

B.1	Linear fit of parameters from Langmuir adsorption model (presented in Tables B.1, B.2 and B.4), the isosteric heat is found as the slope of the line. 20 nm silica NPs by (a) procedure 1 and (b) procedure 2 (LSPR response in Appendix A.3), (c) 7 nm NPs and (d) 20 nm NPs, both deposited by procedure 2 (LSPR response in Figures 6.8a and 6.8b), (e) 7 nm and (f) 20 nm NPs, control measurement by procedure 3 (LSPR response in Appendix A.4).	IX
B.2	Linear fit of parameters from Langmuir adsorption model (presented in Tables B.5 to B.7), the isosteric heat is found as the slope of the line. First samples of (a) monoamine and (b) triamine functionalization deposited by procedure 2 (LSPR response in Figure A.5), second sample of (c) monoamine and (d) triamine functionalization, deposited by procedure 2 (LSPR response in Figure A.6), (e) monoamine and (f) triamine, deposited by procedure 3 (LSPR response in Figures 6.12a and 6.12b).	X
C.1	7 nm silica NPs deposited by procedure 3, imaged at 70° angle. One can see that it is indeed a thick layer.	XI
C.2	20 nm silica NPs deposited by procedure 1 on (a) Si wafers and (b) Si wafers coated by 10 nm Si ₃ N ₄ . In (a) a fairly thick is deposited, in (b) is the thickness varying from really thick to less than a monolayer.	XI

List of Tables

B.1	The parameters obtained from the Langmuir fitting of the data from the CO ₂ adsorption measurement of bare 20 nm silica NPs deposited by procedure 1 and 2 respectively, LSPR response in Appendix A.3.	V
B.2	The parameters obtained from the Langmuir fitting of the data from the CO ₂ adsorption measurement of bare 7 nm and 20 nm silica NPs deposited by procedure 2, LSPR response in Figures 6.8a and 6.8b.	V
B.3	The parameters obtained from the Langmuir fitting of the data from the CO ₂ adsorption measurement of bare 7 nm and 20 nm silica NPs deposited by procedure 3, LSPR response in Figures 6.9a and 6.9b.	VI
B.4	The parameters obtained from the Langmuir fitting of the data from the control measurement of CO ₂ adsorption on bare 7 nm and 20 nm silica NPs deposited by procedure 3, LSPR response in Appendix A.4.	VI
B.5	The parameters obtained from the Langmuir fitting of the data from the measurement of amine modified silica deposited by procedure 2, the first samples, LSPR response in Figure A.5.	VI
B.6	The parameters obtained from the Langmuir fitting of the data from the measurement of amine modified silica deposited by procedure 2, the second samples, LSPR response in Figure A.6.	VII
B.7	The parameters obtained from the Langmuir fitting of the data from the measurement of amine modified silica deposited by procedure 3 yielding a thicker layer, LSPR response in Figures 6.12a and 6.12b.	VII

1

Introduction

That global warming is caused by emissions of CO₂ and other green house gases is undebatable. Islands in the Pacific Ocean, such as the Tuvalu or the Kiribati Islands, risk to sink entirely when the ocean level rises. During 2015, we experienced more extreme weather than ever before. It was the hottest year ever recorded and natural disasters as floods, storms and wildfires were reported far too often. But hope is spiring after the climate congress in Paris in December 2015, where World leaders decided to take severe action against climate change.

Renewable energy is of course the best solution and necessary for a sustainable society. But coal-fired plants are still used and will be for at least one or two decades more. Today, fossil fuel power plants account for more than one third of the total CO₂ emissions [1]. Other large point sources are industries where CO₂ is produced as a by-product, such as cement production, ammonia synthesis, fermentation processes and hydrogen production from carbon sources [1]. There is the CO₂ content of the flue gas often high, which is favorable as capturing CO₂ is less energy demanding at high concentrations. Carbon dioxide Capture and Storage (CCS) is a possible solution to decrease the release of CO₂ into the atmosphere, from all of these sources. CCS means to selectively collect CO₂ from the exhaust gas mixture and pressurize it. The collected CO₂ could either be transported to a permanent storage, e.g. geological storage (such as oil or gas fields) or ocean storage, or be reduced to carbohydrates. By photocatalysis, either in hydrogen containing gas phase or water phase, CO₂ could be reduced to carbohydrates such as methane or ethanol and be a sustainable substitute to fossil fuels [2, 3].

The most developed CCS techniques so far are all based on amine containing liquids. With technology available already in 2005, 85-95% of the CO₂ from a power plant could be captured [4]. But the energy demands were high, for coal-fired power plants the total energy usage would increase with 24-40% [4]. The CO₂ capturing process is highly energy demanding, together with compression of the CO₂, it accounts for 70-90% of the total energy consumption of CCS [5]. In the liquid amine approach, separating CO₂ from the liquid is particularly energy demanding. Another approach that has gained more attention during the past few years is mesoporous systems with high surface area. Zeolites, used in catalysis, have also been investigated for CCS, along with metal-organic frameworks and mesoporous silica (SiO₂) systems. To separate CO₂ from these solid supports requires less energy than from liquid sorbents and is more volume efficient. Using colloidal silica as a solid sorbent is investigated in this thesis. A more thorough presentation of the state-of-the-art of silica as a

CCS sorption material is given in Chapter 2. There are commercially ready-made mesoporous silica systems, however, these are expensive. Therefore, the colloidal silica NPs provided by AkzoNobel Pulp and Performance Chemicals AB are tested in this thesis, as it offers a cheap and already available substitute. These colloidal particles are solid and nonporous, the high surface area is provided by the high surface-to-bulk ratio rather than pores in the particles themselves.

The sorption material needs to have high affinity to CO_2 , in order to selectively adsorb it rather than other gases. After CO_2 is captured from the flue gas, it is usually separated from the sorption material by a pressure or temperature swing, where either the pressure or temperature is changed cyclically. Thus, for this process to be efficient, the binding energy should not be too high. Governing these properties is the *isosteric heat of adsorption*, Q_{st} . Thus, to optimize this factor is crucial in the search for a suitable sorption material. Traditionally, volumetric or gravimetric measurement principles are used to determine the isosteric heat. However, both of these measurement methods require calibrations. The former requires determination of the void volume in the system and the latter requires the skeletal volume, that is the entire solid volume minus the void volume [6]. When measuring over a large temperature range, these volumes will in reality change and induce errors in the measurement results. By instead measuring the adsorption optically, no calibration is needed and the volume change will not be a problem. The optical technique used in the thesis work is known as Indirect Nanoplasmonic Sensing (INPS). It is based upon plasmonic nanostructures placed on a glass substrate. INPS has been showed successful for detection of CO_2 and H_2 [7, 8] and other similar optical techniques have also been proven successful for gas detection. The principle is thoroughly explained in Section 3.3.4.

Purpose of this thesis

To find a way of capturing CO_2 is of great interest in order to lower the amount of released greenhouse gases. One possible technology subject to a lot of research is based upon mesoporous silica structures. This project aims to investigate the possibilities of using commercial colloidal silica nanoparticles from AkzoNobel Pulp and Performance Chemicals AB for capturing CO_2 . The main objective of the study is to find out whether colloidal silica nanoparticles are a suitable sorption material for CCS. Along with evaluating the suitability of INPS for studying this type of system. In addition, amine functionalized silica is studied, to see if this enhances the adsorption capacity, as seen in other works. Two sizes of silica particles are studied, 7 nm and 20 nm.

The second objective of the thesis is to find a reproducible method for depositing the silica nanoparticles onto the sensors, in order to obtain reliable results from the gas adsorption measurements. As this system has not previously been studied as a sorption material for CCS, this accounts for a considerable part of the work. This knowledge will be of use in future studies of the colloidal silica nanoparticles.

2

Carbon dioxide Capture and Storage

This chapter provides an introduction to state-of-the-art in Carbon dioxide Capture and Storage (CCS), particularly to mesoporous silica systems. Even though, the main focus of the theoretical background rather is on the physical principles behind the experiments than CCS. This chapter aims to give the reader a background on the current developments using amine functionalized silica supports for CCS.

2.1 The principle of Carbon dioxide Capture and Storage

There are essentially three ways of capturing CO₂. In *post-combustion*, CO₂ is separated from the flue gas resulting from conventional oxidation. In *pre-combustion* the carbon fuel is oxidized in two steps resulting in a mixture of H₂ and CO₂, by separation of CO₂ only hydrogen is left for combustion. The final technique is known as *oxy-combustion* where the oxidizing agent is high purity O₂ giving a flue gas that mainly contains CO₂ and H₂O, from which separation of CO₂ is significantly easier. The latter technique is the least developed of the three. As this work is a type of post-combustion the focus from now on will be on this type of capture technique.

The principle that is tested in most of the projects run today, are based upon liquid adsorption using amine-based solvents. The most commonly used solvent is monoethanolamine (MEA) [1], which requires a lot of energy upon separation from CO₂. A lot of research is focused on finding more efficient and cost-effective alternatives. Another approach involves solid sorbents instead of liquids. Mostly used is zeolite, which is an aluminosilicate mineral that forms mesoporous structures with high specific surface areas, developed for catalysis. Another mesoporous material in use is silica, which often is functionalized with amine groups to increase affinity to carbon dioxide. One advantage of using a mesoporous structure for adsorption is larger specific surface area for separation, thus, decreasing the entire separation volume. MEA is heated during regeneration, which demands a lot of energy due to high heat-capacity of liquid amine [9] and high water content. If using solid sorbents, one will circumvent this problem, which gives the opportunity of reduced energy demands.

In literature, both zeolites and mesoporous silica have been tested for adsorption

of CO₂. With moisture present in the flue gas, a hydrophilic sorbent will likely perform worse than a hydrophobic one, since water will compete with CO₂ at the binding sites. Zeolites are hydrophilic and perform worse when there is water vapor in the flue gas. Lu et al used Mesoporous Spherical-Silica Particles (MSP) with a specific surface area of 1129 m²/g and compared the amount of adsorbed CO₂ for N-[3-(trimethoxysilyl)propyl]ethylenediamine (EDA)-modified MSP to that of EDA-modified zeolite [9]. They found that EDA-modified MSP adsorbed approximately the double amount per sorbent weight. In the next section amine functionalization of silica is discussed in more detail.

2.2 Amine functionalized silica for CCS

In literature, different porous silica structures are investigated as well as various amine functionalizations. One frequently used functionalization is polyethyleneimine (PEI). Sakpal et al compared the adsorption capacity of bare silica gel and gel functionalized with either PEI or (3-aminopropyl)triethoxysilane (APTS) [10]. APTS is an aminosilane, in other words a silicon atom connected to four hydrocarbons, where one is ending with an amine group. APTS along with a linear PEI are shown in Figures 2.1a and 2.1b. Sakpal et al found that PEI had higher capacity of adsorbing CO₂ than APTS at 2.5 MPa and 3.5 MPa. At atmospheric pressure, however, the capacities were comparable. This indicates that the pressure affects the ability to adsorb CO₂, thus, the functionalization needs to be optimized for the environment it is supposed to work in.

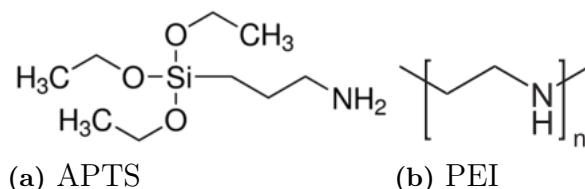


Figure 2.1: Common molecules used for functionalization of porous silica support structures to enhance CO₂ adsorption. (a) APTS ((3-aminopropyl) triethoxysilane) and (b) PEI (polyethyleneimine).

Ready-made mesoporous silica support materials are commercially available, such as SBA-15 and MCM-41, but are expensive. The silica support can account for as much as 90% of the total sorbent cost, as it can cost more than 700 US\$/kg [11]. Therefore, if possible, it is a good idea to use a cheaper but also commercially available material, such as the colloidal silica from AkzoNobel PPC AB that is investigated in this thesis. Unlike the mesoporous silica systems found in the literature with common particle sizes in the micrometer range, these colloidal silica nanoparticles are nonporous. The high specific surface area instead originates from the high surface-to-bulk ratio due to the nanometer scale of the particles. Zhang et al tested several combinations of gel particle sizes (33-425 μm), these are indeed three orders of magnitude larger than the colloidal silica tested in this thesis, pore

volumes ($0.68\text{--}1.15\text{ cm}^3/\text{g}$) and PEI molecular weights and loadings [11]. They found that the optimal PEI molecular weight was the lowest out of the tested weights: 423, 25,000 and 50,000 M. They found no gain in loading more than 50 wt% PEI, since the pore volume was filled at this loading and excessive PEI would only bind to external surfaces of silica gel.

The loading amount and the heterogeneity of the amine functionalization can affect the adsorption capacity. Both Danon et al and Bacsik et al have found evidence for chemisorbed CO_2 on amine functionalized silica systems by using Fourier Transform Infrared (FTIR) spectroscopy [12, 13]. In the absence of water carbamates form, with water present hydrocarbonates form instead. Both identified CO_2 bound as alkylammonium carbamates at room temperature, however, Danon et al also found surface-bound carbamates, which they believe to be stronger a bond, as they could not evacuate it at room temperature. Because decreasing the CO_2 pressure does not desorb all chemisorbed species, a slight decrease in capacity is observed if trying to use a pressure swing for desorption, instead a temperature swing would be more suitable. Both groups found differently adsorbed species depending on the amine loading and the heterogeneity of propylamines on the surface (both functionalized by molecules similar to APTS). It is easy to visualize that two chains in close contact are needed to form alkylammonium carbamate, thus the loading matters for the type of species that forms. Bacsik et al also found that higher degree of heterogeneity promoted alkylammonium carbamates. The ratio of physisorbed to chemisorbed CO_2 is temperature dependent, as there is less physisorption at higher temperatures. Apart from the amine loading it is also showed that the length of the alkyl chain affects the efficiency of adsorbing CO_2 . Brunelli et al [14] found that a propylamine gives 20% higher efficiency than using an ethylamine.

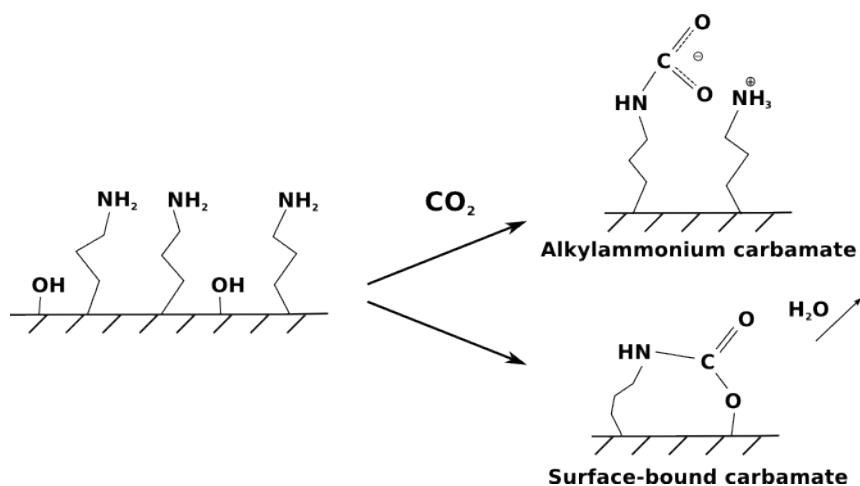


Figure 2.2: To the left, a surface functionalized by alkyl chains terminated by amine groups. To the right, two different types of chemisorbed CO_2 that may form depending on the amine loading and heterogeneity of the loading. Shown above is the alkylammonium-carbamate ion pair and below the surface-bound carbamate.

2. Carbon dioxide Capture and Storage

3

Theoretical background

Theory relevant for the thesis, additional to that given in previous chapter about amine functionalized silica, is given here. This chapter includes the theory of electrical double layer in solution, which describes the stability of colloidal silica particles. This is important because when changing the pH, the silica particles can form a gel. The Langmuir model for adsorption of molecules on a surface is explained, as well as how to estimate the isosteric heat of adsorption from the Gibbs free energy. To measure and optimize the heat of adsorption for CO₂ in the sorption material is of importance for the separation process. Furthermore, a theoretical model of electrons in a metal is described and also the plasmonic properties of nanoparticles, which makes LSPR sensing possible and in particular INPS, which is used in this project.

3.1 Charged particles in solution

The theory of electrical double layer around charged particles in solution is presented in this section, because it is relevant for the stability of colloidal silica particles in solution. Along with specific information about colloidal silica particles and at what pH values the solution is stable.

3.1.1 Electrical double layer

There are several models available for describing the layer of ions forming at surfaces in solution. Most common models for describing the interaction between ions and surfaces are the Helmholtz layer of adsorbed counterions, also known as the Stern layer, and the Gouy-Chapmans diffuse layer. When combining these two models, a good description of the electrical double layer is obtained, which is depicted in Figure 3.1. Helmholtz assumes counterions adsorbed by electrostatic force on the surface. Whereas in the diffuse layer, a higher concentration of counterions is found in the region closest to the surface compared to bulk solution. This region is defined by the Debye length $1/\kappa$, which is to be interpreted as the depth into solution at which no surface effects any longer are found.

The spherical Poisson-Boltzmann equation describes the electric potential $\psi(r)$ for a charged spherical particle in solution.

$$\frac{1}{r^2} \frac{\partial}{\partial r} \left(r^2 \frac{\partial \psi}{\partial r} \right) = -\frac{ze\rho_0}{\epsilon\epsilon_0} e^{-ze\psi/k_B T} \quad (3.1)$$

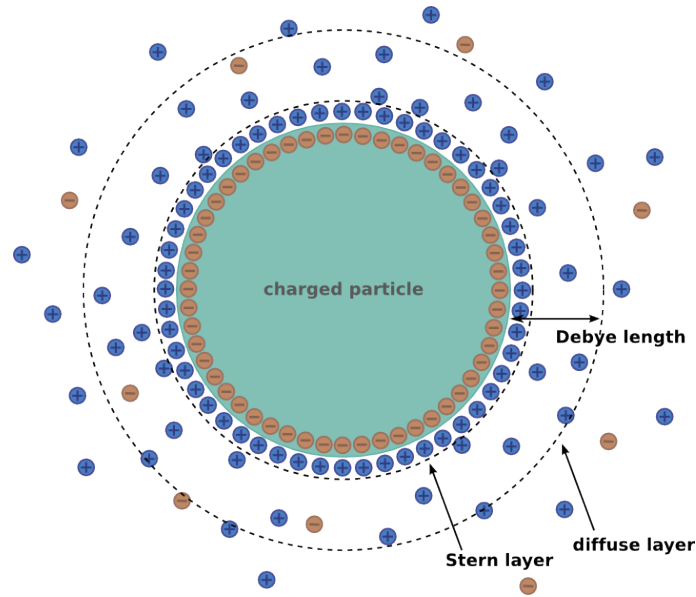


Figure 3.1: Schematic figure explaining the model of an electrical double layer around a charged particle in solution. The model is a combination of the Helmholtz counterion layer, also known as Stern layer, and the Gouy-Chapman model of a diffusive layer.

The origin $r = 0$ is defined as the center of the particle, ρ_0 is the ion concentration where no surface effects are present, e is the elementary charge, ϵ and ϵ_0 are relative permittivity of the solution and vacuum permittivity respectively, z is the valency of counterions in solution, k_B is Boltzmann's constant and T is the temperature in solution. When the surface concentration is low, i.e. the electric potential ψ_0 at the surface is small, the Poisson-Boltzmann eq. (3.1) can be linearized according to

$$\frac{1}{r^2} \frac{\partial}{\partial r} \left(r^2 \frac{\partial \psi}{\partial r} \right) = \kappa^2 \psi \quad (3.2)$$

where $1/\kappa$ is the Debye length, as mentioned before. Assuming only one type of counterions with valence z , we have

$$\kappa^2 = \frac{2ze^2\rho_0}{\epsilon\epsilon_0k_B T}. \quad (3.3)$$

The counterion concentration away from the surface $\rho(r)$ is obtained by solving the Poisson-Boltzmann eq. (3.1), which is a combination of the Boltzmann distribution of counterions in solution $\rho(r) = \rho_0 e^{-ze\psi/k_B T}$ and the Poisson equation of excess charge density. The solution to (3.1)

$$\psi(r) = \psi_0 \frac{a}{r} e^{-\kappa(r-a)} \quad (3.4)$$

is fulfilling the boundary conditions $\psi(a) = \psi_0$, a is the radius of the sphere, and $\psi(r = \infty) = 0$. Giving the counterion distribution as

$$\rho(r) = \rho_0 \frac{1}{\cos^2(\kappa r)}. \quad (3.5)$$

There are two extreme cases to be considered, namely $\kappa a \gg 1$, where the sphere is much larger than the Debye length and the opposite case $\kappa a \ll 1$. In the first case the potential tends to that of a planar surface, where the surface potential is given by $\psi_0 = \sigma/\epsilon\epsilon_0\kappa$. In the latter case, the potential behaves as a Coulomb potential from a charged particle, at distance a from the origin $\psi_0 = Q/4\pi\epsilon\epsilon_0a$, where Q is the total surface charge.

3.1.2 Colloidal silica

The name silica refers to silicon dioxide (SiO_2) and colloidal silica generally means a colloidal phase of silica in either gas or solution. The term also requires the particles to be in the nanometer range. Common forms of colloidal silica are silica gels, powders or, as mainly considered in this thesis, a dispersion of silica particles in solution. From now on when colloidal silica is mentioned it refers to a dispersion of silica particles. A colloidal phase of solid particles in solution is also known as a sol, thus this is a silica sol. Silica has numerous areas of use due to its many favorable properties such as nontoxicity, high abundance in the crust of the Earth and considerable hardness. Which means it is a suitable material for numerous applications, for example it is widely used in paper industry and food industry, or in surface polishers or adhesives.

Silica can appear either in crystalline or amorphous phase. In bulk, each silicon atom binds to four oxygen atoms, which in turn are shared at the most with three other silicon atoms. On the surface, however, this is generally not true as the silicon atoms bind to fewer oxygen atoms and often in solution the surface is hydrated.

The stability of the colloid is governed by the electrical double layer forming around a particle dispersed in solution. The thickness of this layer depends on the pH and the ion concentration of the solution. When the layer is thick enough, the sol remains stable and particles are freely dispersed, but if the layer is too thin they aggregate. At pH higher than 8, the sol is stable due to the electric double layer. If pH decreases it will rapidly aggregate and form a gel, with fastest aggregation usually around pH 6. The isoelectric point, where the net charge of particle and double layer is zero, is found at pH 2, where it once again is more stable [15].

3.2 Calculating the isosteric heat of adsorption

As mentioned in the Introduction, the isosteric heat of adsorption is a crucial factor in the search for the optimal sorption material. Thus, this quantity needs to be determined. It can be done by fitting the data to the Langmuir adsorption model and extracting the isosteric heat from the Van't Hoff equation. The theory behind the calculations are explained below. A brief description of the difference between chemisorbed and physisorbed species is also provided, since both types of adsorption will be dealt with in this thesis.

3.2.1 Chemisorption and physisorption

The adsorption of molecules on a surface are divided into two different categories depending on the strength and the nature of the bond, namely chemisorption and physisorption. Chemisorption is characterized by a covalent bond between the adsorbate and the surface. A chemical reaction occurs when the bond is formed and electrons are transferred either from the adsorbate to the surface or in the opposite direction. Physisorption is characterized by a van der Waals bond which is weaker than the covalent bond, thus physisorbed species are less stable at ambient temperatures. No electron transfer occurs in this binding process. The limit between physisorption and chemisorption can be somewhat diffuse, however as guideline one can have these values for the binding energy; $E_{phys} < 30$ kJ/mol and $E_{chem} > 100$ kJ/mol for physisorption and chemisorption respectively [16].

3.2.2 Langmuir adsorption model

The Langmuir adsorption model treats localized adsorption of molecules on a solid surface. This model is commonly used because it can explain experimental in a wide range of fields. In the Langmuir framework, the system is assumed to be in equilibrium, i.e. the adsorption and desorption flux are equal. For adsorption from gas phase, the adsorption flux is assumed to be proportional to the pressure of the gas, times the number of available sites for molecules to adsorb. It can be written as $K_{ad}P(1 - \theta)$, where θ is the relative coverage and K_{ad} is the rate constant of adsorption. The desorption flux is only proportional to the number of occupied sites, i.e. the relative coverage, thus equal to $K_{de}\theta$, where K_{de} is the desorption rate constant. Assuming these two fluxes are equal at equilibrium gives the Langmuir adsorption model

$$\theta = \frac{\Gamma}{\Gamma_{\infty}} = \frac{KP}{1 + KP} \quad (3.6)$$

where Γ is the coverage on the surface, Γ_{∞} is the maximum possible surface coverage, P is the bulk pressure of adsorbing gas and $K = K_{ad}/K_{de}$ is the ratio between rate constants of adsorption and desorption. As the pressure increases to infinity does the coverage approach $\theta = 1$, indicating fully occupied sites. Eq. (3.6) is valid at constant temperature, thus useful for analyzing isotherms of adsorption processes.

3.2.3 Isothermic heat by the Gibbs-Helmholtz equation

When adsorbing CO₂ the heat of adsorption needs to be optimized to have an efficient process of separating CO₂ from flue gas. The isosteric heat of adsorption Q_{st} is an estimation of the binding energy and is calculated as the enthalpic difference between molecules in gas phase and adsorbed state. One method for calculating this difference in enthalpy is by using the Gibbs-Helmholtz equation. It gives the difference in Gibbs free energy ΔG for a temperature change in the system. The equation is valid under constant pressure, and is given by

$$\left(\frac{\partial(\frac{\Delta G}{T})}{\partial(\frac{1}{T})}\right)_p = \Delta H \quad (3.7)$$

where ΔH is the change in enthalpy, which is negative for an exothermic reaction. Using that $\Delta G = -RT \ln K$ where R is the gas constant, this equation can be rewritten as

$$\left(\frac{\partial \ln K}{\partial(\frac{1}{T})}\right)_p = -\frac{\Delta H}{R} \quad (3.8)$$

which is known as the Van't Hoff equation. K is an arbitrary chemical equilibrium constant. However, if choosing to use the adsorption equilibrium constant $K = K_{ad}/K_{de}$ described in the previous section, the heat of adsorption can be calculated. Since adsorption is an exothermic process, energy is released, thus, temperature changes while pressure is constant, which is why it is called isosteric heat of adsorption. Larger gain in enthalpy by adsorption gives larger isosteric heat as $Q_{st} = -\Delta H$.

3.3 Nanoplasmonics

In this section an introduction to the theory of plasmonics and in particular plasmonic nanoparticles is given, in order to provide the reader with adequate background knowledge. The idea of optical plasmonic sensing is introduced, as it is the main method used for monitoring CO₂ adsorption in this thesis.

3.3.1 Harmonic model of electrons in metals

To understand the plasmonic properties of a metal we start with a simple model of an electron as a harmonic oscillator. This model is more known as the Lorentz model. The electron is displaced by an externally applied field $\vec{E}(\vec{x}, t)$ and the restoring force from the positively charged core pulls it back again, which drives it to oscillate around its equilibrium position. This motion can be described by Newton's equation of motion

$$m_e \frac{\partial^2 \vec{x}}{\partial t^2} + m_e \Gamma \frac{\partial \vec{x}}{\partial t} = e \vec{E}_0 e^{-i\omega t} \quad (3.9)$$

where the charge times the electric field $\vec{E}(\vec{x}, t)$ gives the force, \vec{x} is the displacement of the electron and Γ is the damping of the electrons. Furthermore, the applied field is assumed to be harmonic with frequency ω . Here, the spring constant of the electrons is assumed to be negligible which simplifies the further derivations slightly because the resonance frequency of the oscillator $\omega_0 = 0$. If solving Equation (3.9) for \vec{x} one can write the induced dipole moment as

$$\vec{p} = -e\vec{x} = -\frac{e^2/m_e}{\omega^2 + i\Gamma\omega} \vec{E}. \quad (3.10)$$

Until now, we only considered a system with one electron but we will now extend the system to N free electrons. These constitute what is called the electron cloud. When an attenuating field is applied, the electrons polarize and start to oscillate collectively. We can then define the polarization \vec{P} of the metal as the quantity of dipole moments per unit volume, $\vec{P} = N\vec{p}$. To find a relation for the dielectric function $\epsilon(\omega)$ depending on the frequency, we can use the constitutive relation $\vec{P} = \epsilon_0(\epsilon - 1)\vec{E}$. This will give us the dielectric function for an electron in a metal, also called the Drude model.

$$\epsilon(\omega) = 1 - \frac{\omega_p^2}{\omega^2 + i\Gamma\omega} \quad (3.11)$$

$$\epsilon(\omega) = \epsilon_1(\omega) + i\epsilon_2(\omega) = 1 - \frac{\omega_p^2}{\omega^2 + \Gamma^2} + i\frac{\omega_p^2\Gamma}{\omega(\omega^2 + \Gamma^2)} \quad (3.12)$$

Here the plasma frequency is introduced, which is defined as $\omega_p = \sqrt{Ne^2/m_e\epsilon_0}$. For all frequencies smaller than the plasma frequency the electric field will be reflected at the metal interface, because the electrons can screen the external field fast enough. For bulk metals the plasma frequency is usually in the ultraviolet range, which is why all visible wavelengths are reflected and metal is perceived as shiny and reflective [17].

3.3.2 Quasi-electrostatic approximation

In the previous section, the Lorentz model for electrons in a metal was explained and the plasma frequency introduced. However, in this work the plasmonics of nanoparticle (NP)s are of more interest, therefore the discussion goes on to specific properties of metal nanoparticles. As discussed before, the electrons in a metal can be excited by light and oscillate collectively, this is what is known as plasmonic interaction. On surfaces and thin films, this charge density wave of oscillating electrons along the metal-dielectric interface, also known as a surface plasmon, can propagate in space. However, for a nanoparticle the surface plasmon is confined by the geometry of the particle and thus cannot propagate. Instead, a standing wave is obtained and consequently they are called *localized* surface plasmons. This phenomenon is pictured in Figure 3.2.

Assuming the diameter of the nanosphere is much smaller than the wavelength of the applied field allows us to study the particles as point dipoles rather than a collection of electrons. Thus, only the induced electrostatic field from the polarization \vec{P} needs to be taken into account. The polarization of the dipole can be described as

$$\vec{P} = \epsilon_{med}\alpha(\omega)\vec{E} \quad (3.13)$$

where ϵ_{med} is the dielectric constant of the surrounding medium and $\alpha(\omega)$ is the dipole polarizability describing the interaction between light and the nanoparticle, in other words how easily it is polarized. In Mie theory Maxwell's equations are solved for a nanosphere, yielding an expression for the polarizability $\alpha(\omega)$ of a nanosphere.

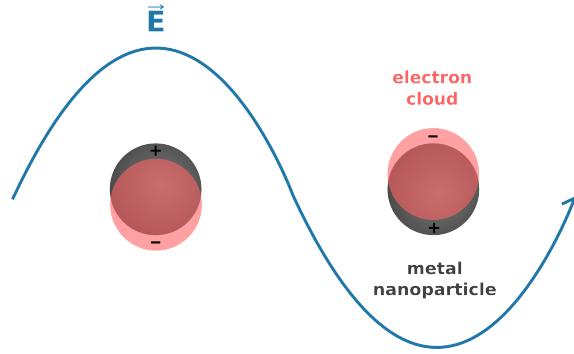


Figure 3.2: Excited localized surface plasmon. An externally applied field, with wavelength $\lambda \gg r$, where r is the nanosphere radius, can excite the free electron cloud of the particle and make it oscillate. Thus, the nanoparticle turns into a time-dependent dipole, which is called a localized surface plasmon, because it is confined by the geometry of the sphere.

$$\alpha(\omega) = 4\pi r^3 \frac{\epsilon_{part}(\omega) - \epsilon_{med}}{\epsilon_{part}(\omega) + 2\epsilon_{med}} \quad (3.14)$$

where r is the radius of the particle. The resonance frequency is found when the losses are at minimum, in other words when $\alpha(\omega)$ is at maximum, which is obtained for $\epsilon_{part} + 2\epsilon_{med} = 0$. Since $\epsilon_{part}(\omega)$ is complex and ϵ_{med} is real, we need the imaginary part $\epsilon_2(\omega)$ of ϵ_{part} to be small and the real part $\epsilon_1(\omega) = -2\epsilon_{med}$. By assuming optical conditions $\omega \gg \Gamma$, we can approximate

$$\epsilon_1(\omega) \approx 1 - \frac{\omega_p^2}{\omega^2} \quad (3.15)$$

which yields the final condition for the resonance frequency of the nanoparticle

$$\omega_{LSPR} = \frac{\omega_p}{\sqrt{1 + 2\epsilon_{med}}} \quad (3.16)$$

or rather as the resonance wavelength will be of more interest for the present work

$$\lambda_{LSPR} = \lambda_p \sqrt{1 + 2\epsilon_{med}}. \quad (3.17)$$

At the resonance frequency the extinction, i.e. the sum of absorption and scattering of light, of the particle is at maximum. Thus, when measuring the extinction spectrum one finds a peak at this wavelength. Since the resonance wavelength depends on the dielectric constant of surrounding medium, see Equation (3.17), it is possible to register changes in the surrounding by studying how the resonance wavelength shifts. This is the idea of Localized Surface Plasmon Resonance (LSPR) sensors.

3.3.3 Localized Surface Plasmon Resonance sensing

Localized Surface Plasmon Resonance (LSPR) sensing is traditionally used within biophysics for detecting the presence of biomolecules. Receptors for a specific biomolecule, e.g. a protein, are immobilized on the NPs of the sensor surface. It is

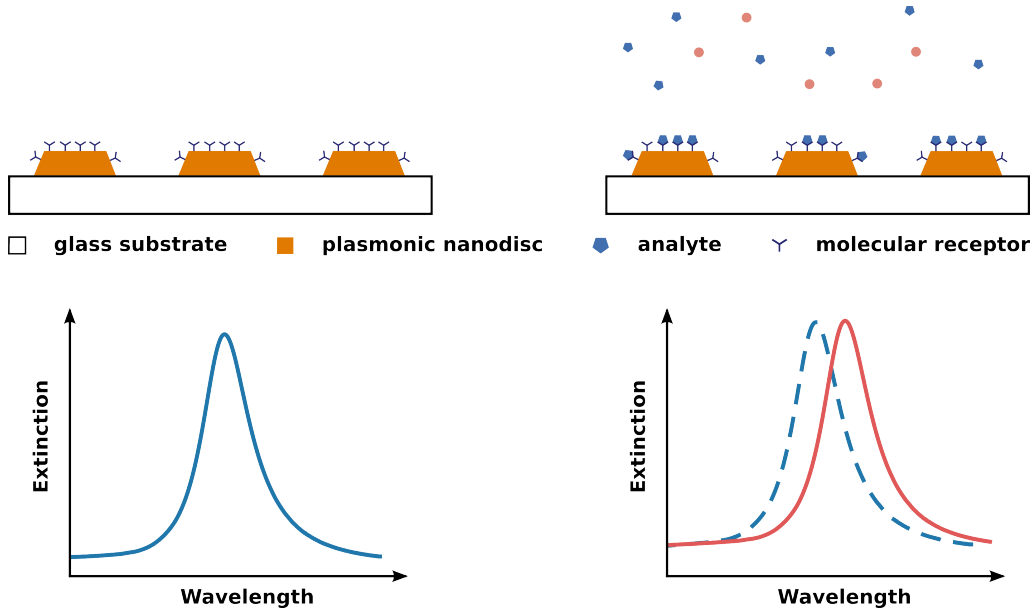


Figure 3.3: Schematic figure illustrating the principle of LSPR sensing. Receptors are immobilized on the nanoparticles and when analytes bind to these the LSPR extinction peak red-shifts due to the increase in dielectric constant of the surrounding medium. The binding event is detected by measuring the extinction spectrum change.

possible to detect when the protein binds to the receptor due to the change in refractive index (RI) of the medium surrounding the plasmonic nanoparticles. Figure 3.3 provides a schematic sketch of how LSPR sensing works. The resonance wavelength of the plasmonic nanoparticles depends on the dielectric constant of surrounding medium as stated by Equation (3.17). The RI is related to the dielectric function as $\epsilon_{med} = n^2$, and the shift in LSPR wavelength is rewritten as

$$\lambda_{LSPR} = \lambda_p \sqrt{1 + 2n^2}. \quad (3.18)$$

For $n > 1$, one can approximate $\lambda_{LSPR} \approx \lambda_p \sqrt{2}n$, thus the LSPR wavelength shift depends approximately linearly on the change in RI

$$\Delta\lambda \approx \lambda_p \sqrt{2}(n_2 - n_1). \quad (3.19)$$

When proteins are adsorbed, the refractive index of the surrounding changes from n_1 to n_2 , yielding a red-shift of the resonance wavelength λ_{LSPR} if $n_2 > n_1$. Thus, by measuring light transmitted through the sensor and calculating the shift $\Delta\lambda$, one can detect when these proteins are present in the solution.

The LSPR is sensitive to other changes than the RI of the surrounding medium. Changes to the nanoparticle itself will yield a shift of the resonance peak, such as shape and size of the nanoparticle or phase changes as oxidation or melting. Using LSPR in this way is known as *direct plasmonic sensing* and has taken plasmonic sensing into the material science field. However, since the shift of the resonance peak is unspecific and can be due to a number of reasons one must be certain to interpret

the results correctly and exclude possible other sources of a resonance shift. This problem is partly minimized by using gold NPs, since it is a noble metal and thus reasonably inert.

Three readouts are possible from the extinction spectrum measurements, additionally to the LSPR wavelength shift $\Delta\lambda$, the peak extinction at the resonance wavelength λ_{LSPR} and the width of the peak are two relevant parameters. Usually, all of them change but depending on the experiment one or more parameters can be studied.

3.3.4 Indirect Nanoplasmonic Sensing

As stated in the previous section, LSPR sensing is unspecific and many factors may contribute to the shift in plasmonic resonance. To eliminate one source of such errors, a dielectric spacer layer of a few nanometers can be deposited on top of the nanoparticles, to hinder physical or chemical interaction between the material of interest and the sensor surface. This method is known as Indirect Nanoplasmonic Sensing (INPS), which refers to that the sensing is only realized through the strong electric field from the nanoparticles. Thus, it is necessary to use a dielectric material for the spacer layer to let the electric field extend through the layer. A schematic figure of the principle is provided in Figure 3.4. This technique lets plasmonic sensing extend beyond the field of biophysics, as showed by Langhammer et al [7] when first published. INPS can be used, among other things, for finding the glass transition temperatures of polymers or studying thermodynamics of hydrogen storage in nanomaterials.

The advantage of INPS is that the spacer layer protects the gold nanodiscs from alloying or oxidation as the material of interest does not directly interact with the nanodiscs. The layer also helps the discs to keep their shape at higher temperatures. The spacer layer can be specifically tailored to provide the surface properties needed in a specific experiment, either as an inert surface to the material of interest or to actively participate in the reaction. More specific information about sensor chip material preparation and dimensions of both nanodiscs and spacer layer will follow in Chapter 4.

Plasmonic sensing provides a highly sensitive approach of detecting gases. It has been shown that it is possible to use INPS for hydrogen sensing [7] and CO₂ adsorption in a polymer network [8]. Similar systems of thin films plasmonically functionalized by embedded nanoparticles has also been used successfully for detecting CO and H₂. Thus, optical spectroscopy for gas detection is a fairly established method.

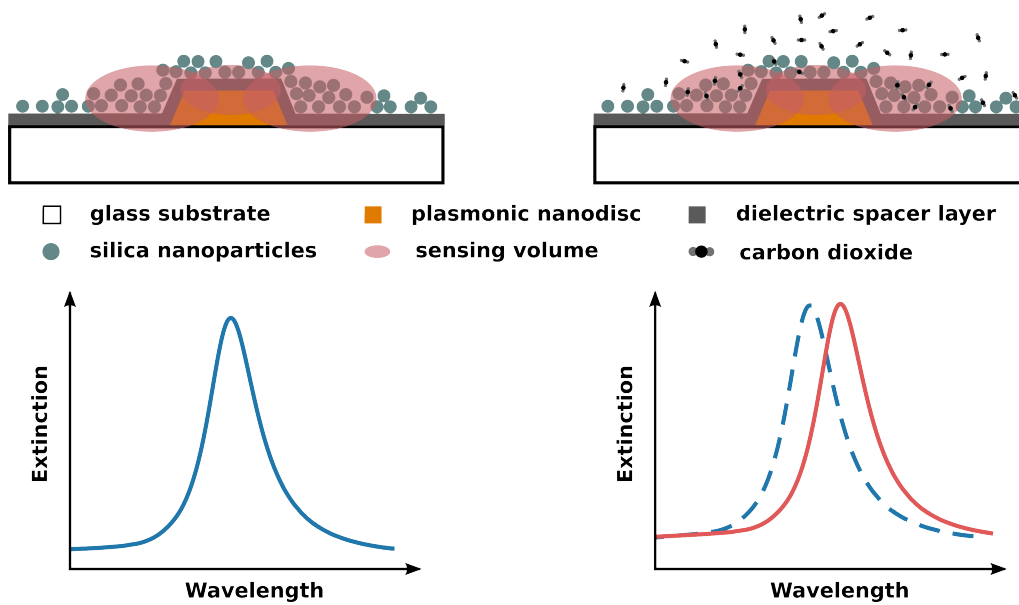


Figure 3.4: Schematic figure illustrating the principle of INPS sensing. INPS is a LSPR technique where the plasmonic particles (here nanodiscs) are covered with a dielectric spacer layer, both to protect them from any interaction with the material of interest and to provided tailored surface properties. Gas adsorbed within the sensing volume of one nanodisc yields a red-shift in plasmonic resonance due to the change in RI.

4

Nanofabrication

Already in 1959 Richard Feynman, through a lecture called “*There is plenty of room at the bottom*”, predicted the many possibilities of nanotechnology. However, it took another 20 years until researchers started to discuss nanotechnology as we think of it today. From then on, paramount progress has been made within the nanofabrication field, that is the fabrication techniques to build structures at the nanometer scale. The enormous progress is apparent in every day life from the decrease in size of computers while their performance improves.

In this project, the indirect nanoplasmonic sensor (INPS) chips used in the CO₂ adsorption measurements were produced by state-of-the-art nanofabrication in the cleanroom at Chalmers. The method is known as Hole-Mask Colloidal Lithography (HCL), which is explained in the next section. When fabricating nanostructures there are two main categories of fabrication techniques; *top-down* and *bottom-up*. In the former one starts with a piece of material and starts cutting or etching it to obtain the final structure, this generally requires advanced equipment such as electron or ion beam lithography. The latter means that you start from a clean surface and build up your structure simply from the bottom up, HCL belongs to this category.

The procedure of depositing the silica particles on the sensor surface will also be described. It is a fairly simple step in the sense that no advanced tools are required. However, it is a crucial step for the reproducibility of the samples and comparison between different measurements.

4.1 Plasmonic sensors produced by Hole-Mask Colloidal Lithography

Hole-Mask Colloidal Lithography (HCL) [18] is a simple method for producing nanodiscs or cones, in quasi-random arrays distributed on a substrate. Thus, it is useful for fabricating plasmonic sensors, which all are comprised of nanoparticles or discs on a glass substrate.

The steps of HCL are depicted in Figure 4.1; to ease the understanding of the process. Firstly, poly(methyl methacrylate) (PMMA) is spin-coated at 2000 rpm for 1 minute on clean glass substrates and baked for 10 minutes at 170 °C. This results in approximately a 200 nm thin film. The PMMA surface is etched with oxygen plasma for 5 seconds (50 W, 250 mTorr), in order to increase the hydrophilicity. A

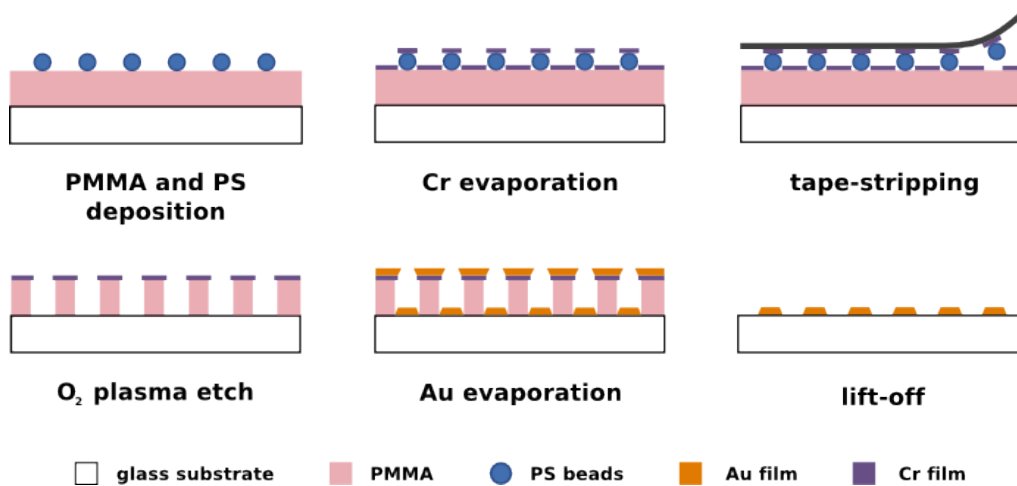


Figure 4.1: Schematic figure of the fabrication steps in Hole-Mask Colloidal Lithography (HCL). First a PMMA layer is spin-coated on the substrate and PS beads are self-assembled on top. A 15 nm Cr thin film is evaporated on the sample, in which holes are made by tape-stripping of the PS beads. Holes in the PMMA are etched by oxygen plasma and a 20 nm Au thin film is evaporated over the sample, which finally is lifted off by dipping into acetone, producing Au nanodiscs.

polyelectrolyte (0.2 wt% PDDA) is drop-coated on the PMMA film to make the surface positively charged. It is incubated for 40 seconds before being rinsed off with de-ionized water and blow-dried with N_2 . It is followed by drop-coating of negatively charged polystyrene (PS) beads (0.02 wt% with diameter 140 nm or 170 nm), incubating for 3 minutes, rinsing with de-ionized water and blow-drying. When drying, it is important to blow from the middle and out, to not let waves of PS beads flow back over the dried surface and give an uneven surface coverage. This should also be considered when blowing after PDDA deposition but is more crucial after PS. On top of the PS beads a 15 nm Cr thin film is evaporated. The PS beads are then removed by tape-stripping, creating holes in the Cr film, which acts as the mask for the nanodiscs. The samples are etched once more with O_2 plasma, but for 5 minutes this time, to remove the PMMA in the holes of the Cr mask. A 20 nm thick Au film is evaporated on top of the hole-mask, creating nanosized discs inside the holes. Thus, the size of the discs is controlled by the diameter of the PS beads and the sides of the discs will be slightly inclined because the opening of the hole shrinks during evaporation. Finally, the mask is lifted off by dipping the samples into acetone, which desolves the PMMA and only the Au nanodiscs on the glass substrate remain.

4.2 Chemical vapor deposition of dielectric spacer layer

As explained in Section 3.3.4, a dielectric spacer layer is needed both to protect the Au nanodiscs from reshaping and to provide a chemically appropriate (inert in my case) surface. It is necessary to use a dielectric material to let the electric

field extend beyond this layer. The spacer layer was deposited by Plasma Enhanced Chemical Vapor Deposition (PE-CVD). Two different materials were tested at the beginning of the project, namely SiO_2 and Si_3N_4 , from which the latter was chosen since it gave a more inert surface; more about this in Chapter 6. There is a trade-off concerning the thickness of the layer; it needs to be thick enough to cover the entire surface, but thin enough to let the electric field of the plasmonic discs through. It was concluded that 10 nm provided the best compromise, more on this will also be discussed in Chapter 6.

4.3 Silica nanoparticle deposition

The deposition of silica particles onto the sensor chips was a crucial part of the sample preparation, as the coverage on the Au nanodiscs highly affects the results, in particular the magnitude of the wavelength shift $\Delta\lambda_{peak}$ induced by CO_2 adsorption. Different approaches of deposition were tested to find one that would give reproducible results and where the changes of parameters from the gas adsorption measurement could be interpreted. Two standard procedures and one modified procedure combining the advantages of the previous two for obtaining a thicker layer, are presented below. These procedures were followed for the preparation of the samples, whose CO_2 adsorption capability was to be evaluated.

The colloidal amorphous silica particles in aqueous solution were obtained from AkzoNobel PPC AB. Two different sizes of particles were used with average diameter of 7 nm and 20 nm, which are calculated as the equivalent spherical diameter based on surface area measurements (called Bindizil 30/360 and Bindizil 40/130, with $360\text{ m}^2/\text{g}$ and $130\text{ m}^2/\text{g}$ specific surface area respectively). Silica particles with amine functionalization were also provided by AkzoNobel PPC AB. One type where 7 nm silica particles were modified by carbon chains containing one amine group and a second type, similar to the first one with the only difference that the carbon chain had three amine groups. These will from here on be referred to as monoamines and triamines, respectively. No further information can be provided about the nanoparticles or the amine functionalization due to secrecy on behalf of AkzoNobel PPC AB.

The cationic polymer used to attach the silica nanoparticles to the sensor surface was called Anionic Trash Catching (ATC) polymer because of its ability to bind to negatively charged particles and compounds. Both polymer and silica particles were diluted with Milli-Q water.

Standard procedure 1: one layer, using cationic polymer

- drop-coat sensor surface with 1 wt% polymer in Milli-Q water until surface well covered
- incubate for 2 minutes
- drop few milliliters of Milli-Q water to dilute polymer solution
- blow-dry with nitrogen
- repeat same procedure as above for 1 wt% silica nanoparticle solution

Standard procedure 2: five layers of high concentration silica solution, no cationic polymer

- drop-coat sensor surface with 10 wt% silica NPs, until surface well covered
- incubate for 2 minutes
- drop few milliliters of Milli-Q water to dilute
- blow-dry with nitrogen
- repeat same procedure as above, usually 5 times in total to yield enough coverage

Procedure 3, thicker layer: two layers of high concentration silica solution, using cationic polymer

- drop-coat sensor surface with 2 wt% polymer until surface well covered (as in procedure 1 but with higher concentration)
- incubate for 2 minutes
- drop few milliliters of Milli-Q water to dilute polymer solution
- blow-dry with nitrogen
- repeat same procedure as above for 10 wt% silica nanoparticle solution (as in procedure 2)
- repeat entire procedure once to yield two silica and polymer layers in total

When blowing, it is important to try not to let any droplets from the edges roll over the already dried surface, as this will give areas with much thicker silica NP layers and thus uneven surface coverage.

5

Analysis methods

The aim of this chapter is to explain the two main analysis methods used. The first one is the optical CO₂ adsorption measurements performed in a quartz reactor tube. The procedure of this method together with the experimental setup are explained closely in the next section. The second method concerns characterization of the silica particle structure formed on the surface from the different drop-coating procedures. For this purpose Scanning Electron Microscope (SEM) was mainly used. An introduction to the physical principles behind SEM will be given and a brief description of how it was used for this purpose. Additionally, a description of how the extinction spectra were measured is provided.

5.1 Optical CO₂ adsorption measurements: X1 setup

The main objective of this thesis is to investigate and compare the CO₂ adsorption capability of silica NPs with and without amine functionalization. The adsorption capability was measured optically in a gas flow reaction chamber. The samples were INPS chips, fabricated in the cleanroom by HCL explained in Section 4.1, covered with silica NPs deposited as described in Section 4.3. By controlling the temperature of the reactor, it was possible to investigate the temperature dependence of the adsorption, which is necessary to calculate the isosteric heat of adsorption as explained in Section 3.2.

The gas flow reaction chamber Insplorion X1, commercially available from Insplorion AB, was used in the adsorption measurements. Figure 5.1 provides a schematic of the measurement setup. A gas mixture of CO₂ and Ar at 1 atm was flowed through the reaction tube, usually at a flow rate of 100 ml/min. Due to limitations in maximum and minimum flow of the mass flow controllers, sometimes a higher flow was needed, e.g. to achieve 90% partial pressure CO₂ in 10% Ar of 1 atm. As mentioned, Ar was used as carrier gas and the gas composition varied from pure Ar to pure CO₂, including several steps in between. The sample was mounted in the quartz gas reactor aligned with the optical fibers. White light was irradiated through one optical fiber. Transmitted light was collected at the other side and analyzed by a spectrometer. The temperature was controlled by a feedback loop. The temperature of the sample was measured by a thermocouple and the reactor was heated by a heating coil twisted around it. An extinction reference of a clean glass slide was collected before the measurement of the actual samples, apart from

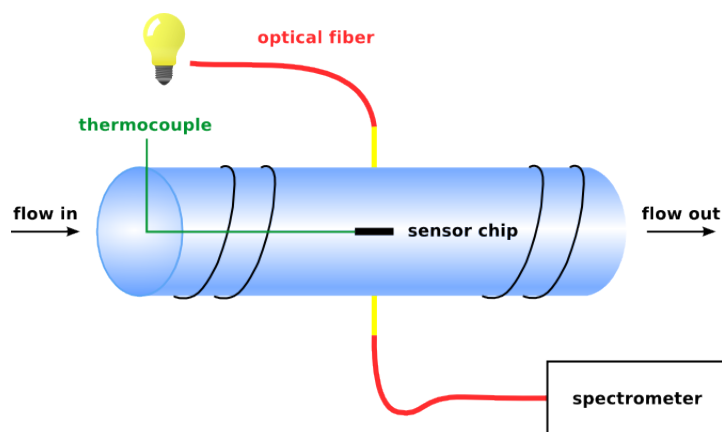


Figure 5.1: Schematic sketch of the measurement setup X1 used for CO₂ adsorption measurements. The sensor chip was mounted in the middle of the reactor, white light irradiated the sample, transmitted light was collected by the optical fiber and analyzed by the spectrometer. The temperature was controlled by a thermocouple.

that was no calibration of the setup needed.

A standard measuring procedure follows:

- heat the reactor to 358 K and wait 1 hour for the sample to stabilize at this temperature e.g. to evaporate possible solvent residuals
- flush the reactor with 100% CO₂, two times for 7.5 minutes and equal time of pure Ar in between
- first series of adsorption measurements: at each CO₂ concentration the gas mixture was flushed for 7.5 minutes and in between pure Ar was flushed for equally long time, the CO₂ levels usually measured were CO₂ partial pressures at 25, 50, 75 and 100% of 1 atm
- decrease the temperature in the reactor to the next level
- repeat from the second point at all temperatures, usually measurement series were taken at the following four temperatures; 358, 338, 318 and 298 K.

5.2 Characterization of silica particle layers by scanning electron microscopy

The structure of the deposited silica layer affected the results obtained from gas adsorption measurements. Thus, it was important to try and achieve a reproducible coverage of the sensor surface to have comparable results. To image the coverage on the substrates Scanning Electron Microscope (SEM) was used. SEM is an imaging technique used to visualize objects below the diffraction limit of optical microscopes at around 200 nm. With SEM it is possible to image objects down to ten nanometers in size.

When imaging by SEM the sample is put in a high vacuum chamber and bombarded by a high voltage electron gun. When the electrons hit the surface different pro-

cesses can occur depending on the substrate. The two main types of processes yield back-scattered electrons or secondary electrons. Back-scattered electrons contain information about the composition of elements on the surface. Secondary electrons come from atoms that absorb the electrons from the beam, they become excited and sequentially emit an electron. The intensity of these secondary electrons will construct the SEM image.

The voltage of the electron beam will decide how far into the substrate one will see, because electrons of higher energy will penetrate deeper into the surface and yield secondary electrons from deeper lying atoms. When imaging it is important that the substrate is conductive and grounded to lead away absorbed electrons, in order to not build up charges. When imaging Si this charge build-up phenomenon is indeed observed since Si is a semi-conductor and even more so when covered by insulating SiO₂. However, it is still possible to image but the area hit by the electron beam becomes lighter. Glass on the other hand, which is used as substrate for the optical sensing, is an insulator and difficult to image. Therefore, it is very hard to use the same substrate as in X1 gas measurements. Instead, silica particles were deposited onto a Si substrate for imaging following the same procedure as when depositing on INPS chips described in Section 4.3.

For imaging a Zeiss Supra 60 VP SEM was used at beam voltage 5 kV. The samples were imaged from above, to see the overall structure and the coverage, if there was a monolayer or several layers. Additionally, the samples were imaged from the side at 70° inclination to visualize the thickness of the layer and how well covered the Au discs of the sensor surface were by the silica NPs.

5.3 Extinction spectrum measurement

To visualize the extinction of the INPS chip and to see the shift in LSPR when adding more silica to confirm that there is indeed more silica on the surface, the extinction spectrum was measured. The spectrometer used was a CARY 5000 UV-Vis-NIR. The sample was mounted in the same position each time, to make sure to measure at the same spot. Transmitted light was collected by the spectrometer and analyzed.

For monitoring silica after each deposition, 20 nm silica NPs were deposited according to procedure 2 described in Section 4.3. Before putting the sample into the spectrometer, it was heated up in an oven at 378 K for 15 minutes, to evaporate any solvent residuals on the surface. Water residues will give rise to errors in the spectrum.

6

Result

This chapter presents the key results obtained during the thesis work. It aims to give the reader a clear view and interesting reading about the main findings of the project. First, several reference measurements are presented. These were performed in order to understand how the sensor chip itself affects the results of the gas adsorption measurements. As mentioned in Sections 3.3.3 and 3.3.4, the LSPR shift is an unspecific read-out, hence, many factors can contribute to the response. Therefore, it is important to eliminate all possible error sources, to ensure that the shift is solely due to adsorption of CO₂ on the silica system. The reference measurements include CO₂ adsorption on gold nanodiscs, on spacer layers of different materials and thicknesses and on the cationic polymer used to bind silica to the sensor surface. In addition, the extinction spectrum of a bare INPS chip, as well as with up to eight depositions of silica particles, are analyzed, to confirm the deposition of silica on the sensor.

In the third and the fourth section, the main findings of the project are presented, including CO₂ adsorption on bare silica NPs and particles functionalized by amine groups, along with SEM images to visualize how the silica NPs cover the INPS surface. Lastly, the isosteric heats of adsorption of CO₂ are presented for the four tested systems and compared to values found in literature. Any further information on the amine functionalization and the amine containing molecules can not be provided due to secrecy on behalf AkzoNobel PPC AB, who have provided the materials.

6.1 Investigating background signal from gold nanodiscs, spacer layer and cationic polymer

Since LSPR is a non-specific method all other factors that may induce a shift in resonance wavelength need to be minimized to be sure the shift is solely due to adsorption of CO₂. The results from analyzing and, ideally, optimizing the background signal are presented in the following sections.

In all the following adsorption measurements, the dimension of the Au nanodiscs are kept constant. They are 20 nm thick and fabricated by HCL using PS beads of 140 nm in diameter, resulting in discs with a slightly smaller diameter. From an SEM image of an INPS surface (Section 6.1) the average disc diameter was calculated as 120 nm, with a distribution from around 115 nm to 125 nm. A comparison with nanodiscs fabricated using PS beads of 170 nm in diameter was performed, this

is displayed in Figures A.1a and A.1b in Appendix A.1.

Before starting with the results of gas adsorption, a SEM image of an INPS surface is showed in Figure 6.1. The gold nanodiscs are fabricated by HCL and coated by 10 nm Si_3N_4 . The discs are approximately 120 nm in size.

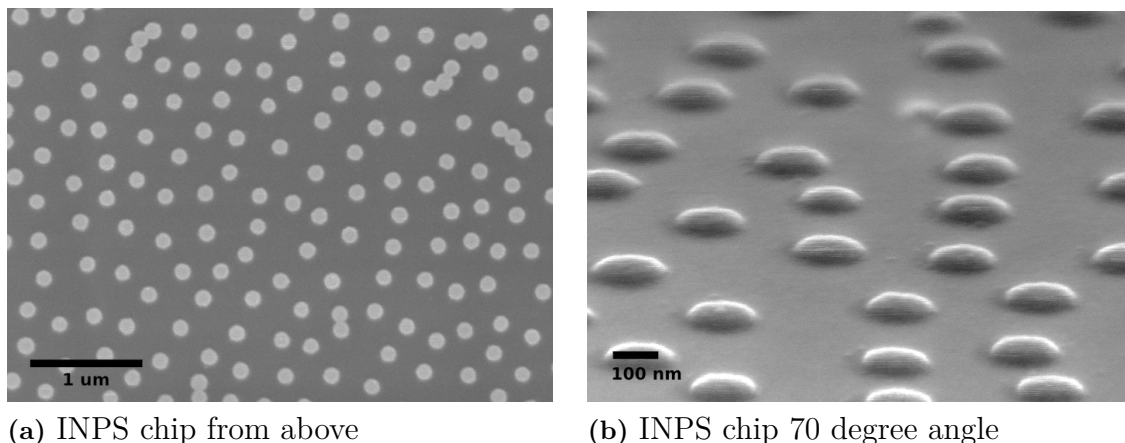


Figure 6.1: The surface of an INPS chip imaged by SEM, (a) from the top and (b) at 70° angle. The gold nanodiscs fabricated by HCL are evenly distributed over the surface. The edges of the discs look smooth due to the Si_3N_4 spacer layer.

6.1.1 Gold nanodiscs

In the process of investigating the effect of the sensor surface on the LSPR shift $\Delta\lambda$, the exposure of bare gold nanodiscs to CO_2 was measured. Solely for this measurement, the glass surface was coated by Si_3N_4 before fabricating the gold nanodiscs, in order to eliminate adsorption on the glass surface which indeed contains silicon dioxide and could possibly adsorb CO_2 . The adsorption of CO_2 was measured in the X1 gas reactor following the scheme described in Section 5.1. At the highest temperature, 358 K, the signal was drifting severely, probably due to reshaping and recrystallization of the gold nanodiscs caused by the elevated temperature. This effect is hindered when covering by a spacer layer, which helps to keep the shape of the nanodiscs. Thus, the measurements at this temperature are not included in the results presented since the error is considered too large. However, the largest $\Delta\lambda$ is always found at the lowest temperature.

In Figure 6.2 we see a considerably large LSPR shift for the CO_2 exposure of bare gold nanodiscs. The cause of this large shift is not obvious. However, further investigation was not necessary since the effect is no longer seen when covering the nanodiscs by the spacer layer (results presented in next section). However, one can speculate about the cause. One simple reason could be that nanosized gold particles are not as inert as bulk gold and CO_2 molecules simply adsorb on the gold discs [19]. Another possible explanation could be the even smaller satellite particles, up to a few nanometers in size, scattered around the nanodiscs from the fabrication.

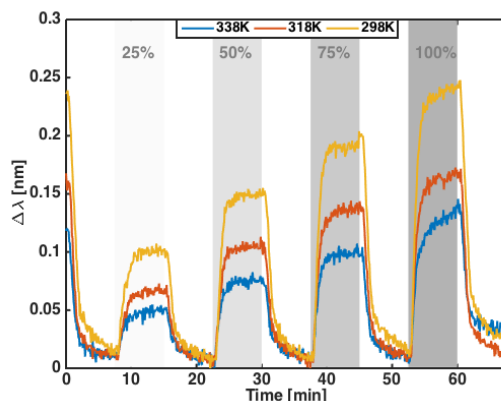


Figure 6.2: LSPR wavelength shift of bare gold nanodiscs. CO_2 was flushed through the reactor during intervals of 7.5 minutes, at partial pressures 25, 50, 75 and 100% of 1 atm (grey fields) at each temperature; 338 K (blue), 318 K (orange) and 298 K (yellow). In between the CO_2 intervals, the system was flushed with pure Ar for equally long time, to desorb the CO_2 .

Since these are much smaller, they should be more reactive and may adsorb carbon dioxide. When covering the discs by the spacer layer, they can no longer interact with the gas or the gold nanodiscs themselves, thus, it is only seen for this case and provides a possible explanation.

In fact, carbon dioxide does indeed adsorb on gold surfaces, as shown by Wu et al [19], using Quartz Crystal Microbalance (QCM). They observed that the adsorption obeys the Langmuir adsorption model, i.e. the adsorption increases at higher CO_2 pressures. This correlates well with the results presented here. However, this adsorption is not a problem in this work, as will be seen in next section, when coating the gold discs by a Si_3N_4 layer, this effect disappears.

6.1.2 Material choice for dielectric spacer layer

The plasmonic Au nanodiscs need to be coated by a dielectric layer as inert to CO_2 as possible. As discussed previously, see Section 3.3.4, the key principle of INPS is sensing solely by the electric field, thus it requires a dielectric material that lets the field penetrate the layer. Two different materials, SiO_2 and Si_3N_4 , were investigated as spacer layer. As a start, a 10 nm thick layer was deposited of SiO_2 and Si_3N_4 on Au nanodiscs. The adsorption was measured as described in section Section 5.1. The scheme for this measurement was as follows; CO_2 flowed through the reactor for 5 minutes in each interval, at all four temperatures, 358, 338, 318 and 298 K and four intervals of increasing CO_2 partial pressures; 25, 50, 75 and 100% of 1 atm. In between each CO_2 interval, the system was flushed with pure Ar for equally long time, to desorb the CO_2 .

The grey fields in Figures 6.3a and 6.3b highlight the CO_2 intervals. When comparing Figures 6.3a and 6.3b, it is clear that the wavelength shift $\Delta\lambda$ is much larger

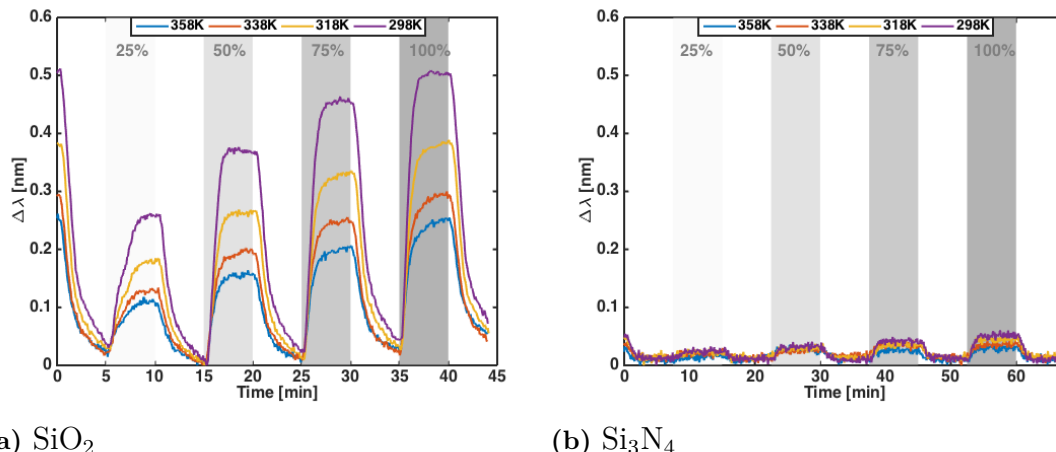


Figure 6.3: LSPR wavelength shift of an INPS chip coated by dielectric spacer layer of (a) 10 nm SiO_2 and (b) 10 nm Si_3N_4 . CO_2 was flushed through the reactor for 5 minutes each time, at partial pressures 25, 50, 75 and 100% of 1 atm (grey fields) at each temperature; 358 K (blue), 338 K (orange), 318 K (yellow) and 298 K (purple). In between the system was flushed with pure Ar for equally long time, to desorb the CO_2 .

for the SiO_2 layer compared to Si_3N_4 , on the order of 10 times larger. The fact that the shift increases when temperature decreases, indicates that the gas actually adsorbs on the surface, according to the Langmuir adsorption model described in Section 3.2.2. When the temperature of the system is higher, the adsorbed molecules will thermally vibrate more and more easily escape from the surface. The Langmuir model assumes equilibrium between adsorption and desorption, when the CO_2 has spread in the flow reactor we assume the system to be in equilibrium, i.e. when the LSPR has stabilized at the new wavelength. Thus, according to the Langmuir model, a higher CO_2 partial pressure yields more adsorption and sequentially a larger LSPR shift.

Since the LSPR shift measured on SiO_2 is tenfold larger than on Si_3N_4 , the latter was chosen for the continued work, which should give significantly less effect on the results. That SiO_2 adsorbs more effectively makes sense since it is the same material as in the silica NPs, which is chosen for adsorption of CO_2 .

6.1.3 Thickness of dielectric spacer layer

The CO_2 adsorption was studied for three thicknesses of Si_3N_4 ; 5, 10 and 15 nm, as seen in Figures 6.4a to 6.4c. Comparing the 5 nm layer with the two thicker layers, a significant difference in LSPR shift is seen. However, between the two thicker layers, 10 nm and 15 nm, there is no noticeable difference of the LSPR shifts.

There is a trade-off concerning the thickness of the spacer layer. Preferably, the

spacer layer is thin. The field from the nanodiscs is strongest in the direct vicinity of the discs and exponentially decays away from it. On the other hand, if the layer is too thin as seen in Figure 6.4a, the LSPR shift is much larger. We cannot be sure of why this is the case, but it might be due to CO_2 molecules diffusing through the thin layer and adsorbing directly on the gold nanodiscs. Or it can simple yield a larger response because the field is stronger closer to the nanodiscs and therefore more sensitive to changes in the RI. Additionally, the sensing volume is larger due to the thinner spacer layer. However, the response is doubled and to be sure that it is not due to the CO_2 exposure additionally to the higher sensitivity, a layer thicker than 5 nm was chosen. It has been seen that the sensitivity with this layer thickness is enough to register the changes upon exposure to CO_2 .

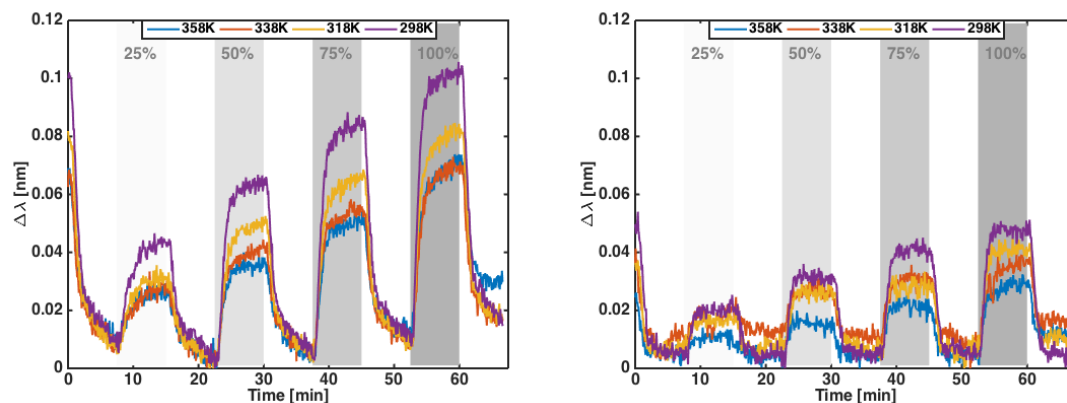
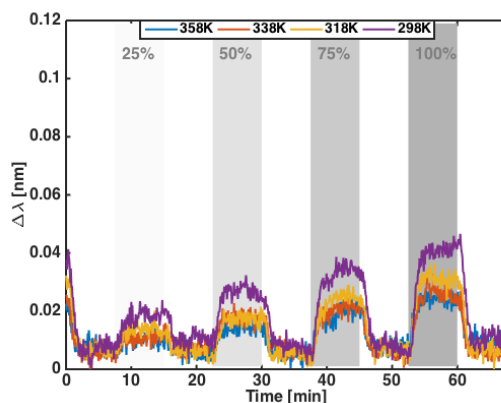
(a) 5 nm Si_3N_4 (b) 10 nm Si_3N_4 (c) 15 nm Si_3N_4

Figure 6.4: LSPR wavelength shift of an INPS chip coated by dielectric spacer layer of (a) 5 nm Si_3N_4 , (b) 10 nm Si_3N_4 and (c) 15 nm Si_3N_4 . CO_2 was flushed through the reactor for 7.5 minutes each time, at partial pressures 25, 50, 75 and 100% of 1 atm (grey fields) at each temperature; 358 K (blue), 338 K (orange), 318 K (yellow) and 298 K (purple).

The shift was smaller for the thicker spacer layers, which gives rise to lower back-

ground signal when running the adsorption measurements on silica nanoparticles. Since no difference was observed between 10 nm and 15 nm Si_3N_4 , the thinner layer of the two was used in the continued work due to the sensitivity of the electric field. This fact also speaks for that the larger shift for the thinner layer is an effect of CO_2 penetrating the layer rather than the higher sensitivity, as there should be a difference also between the two thicker layers in the latter case. Hereafter, all LSPR sensors are coated by 10 nm Si_3N_4 spacer layer even though it is not stated for each sample specifically.

6.1.4 Cationic polymer

CO_2 adsorption on the cationic polymer, used in silica nanoparticle deposition procedures 1 and 3 described in Section 4.3, was measured in the same manner as previous background measurements. Four different partial pressures of CO_2 at four temperatures. In between each CO_2 interval of 7.5 minutes, pure Ar was flushed for equally long time. The LSPR shift from this measurement is seen in Figure 6.5. There is a clear shift when letting on CO_2 (grey fields), but of the same order as for a clean Si_3N_4 surface as in Figures 6.3b and 6.4b. Thus, it is not possible to say from this measurement alone, if there is some adsorption on the polymer or if the response is due to the Si_3N_4 spacer layer beneath. It cannot be concluded that the polymer adds to the LSPR shift. However, since everything added to the sample can cause errors and uncertainty in the interpretations, it is wise to exclude the polymer when possible.

A control measurement showed the same result as presented here, see Appendix A.2. Further investigation of the effect of the cationic polymer was outside the scope of this thesis. However, to use it in silica nanoparticle depositions is assumed to have a negligible effect on the LSPR results.

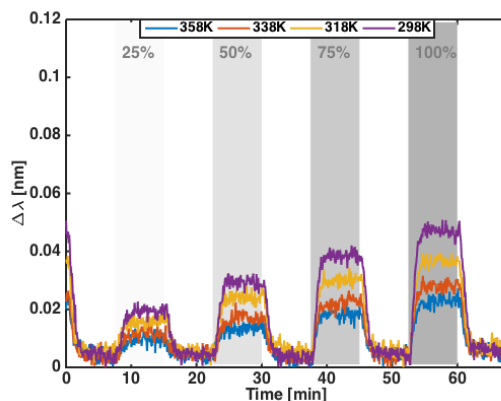


Figure 6.5: LSPR shift $\Delta\lambda$ of cationic polymer on an INPS chip. CO_2 was flushed through the reactor during intervals of 7.5 minutes, at partial pressures 25, 50, 75 and 100% of 1 atm (grey fields) at each temperature; 358 K (blue), 338 K (orange), 318 K (yellow) and 298 K (purple).

6.2 Extinction spectra

The extinction spectrum was measured for a bare INPS chip used in X1 gas adsorption measurements as well as after one up to eight times deposition of 1wt% 20 nm silica particles by procedure 2, i.e. no cationic polymer is added. The spectrometer was a CARY 5000 UV-Vis-NIR. The spectra are shown in Figures 6.6a and 6.6b. The peak of the spectrum for the multiple deposition of silica particles is zoomed in, to show how the LSPR peak shifts. The LSPR peak is slightly red-shifted after depositing more silica NPs on top of the INPS chip. There is also a slight decrease in intensity of the peak.

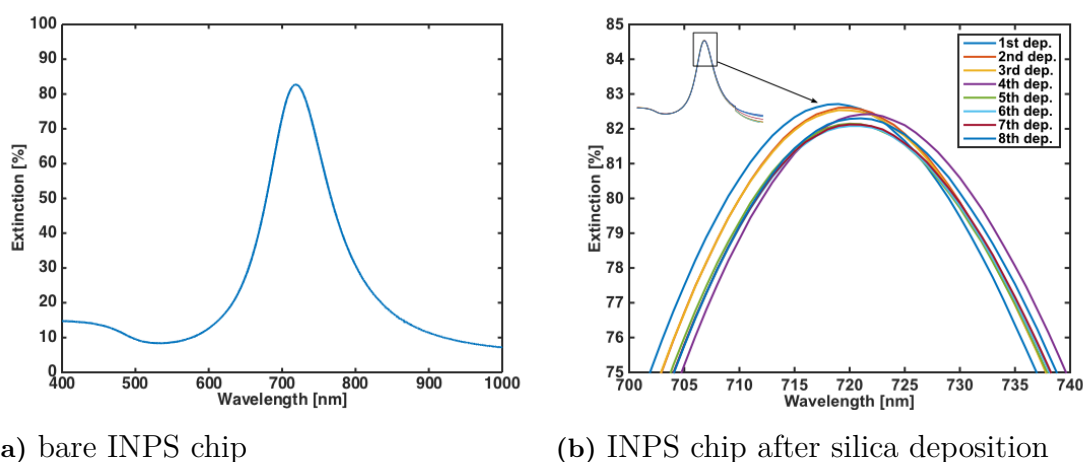


Figure 6.6: Extinction spectrum of (a) a bare INPS chip and (b) an INPS chip coated with 1 up to 8 depositions of 1wt% 20 nm silica particles according to procedure 2.

There is a slight red-shift of the LSPR peak, however, it is not obvious how large or if it is consistent for all depositions. To get a clearer view, the LSPR peak wavelength is showed as a function of the number of depositions in Figure 6.7. The increase in peak wavelength when adding more silica is quite linear, only after the fourth deposition is there a larger shift, which is gone after next deposition. Since, the trend after the fifth deposition once again follows the linear curve this bump is probably due to some water remaining on the surface from the deposition. The samples were heated up for 15 minutes at 378 K to remove water from the surface but probably some water residues were remaining. Since we see the red-shift we can be sure that after each deposition more silica particles are added to the layer and this method is indeed working for covering the sensor surface.

6.3 CO₂ adsorption on silica nanoparticles

When one is convinced the contribution from the INPS sensor to the LSPR shift is small, the results from CO₂ adsorption on silica NPs can be studied. Firstly, bare

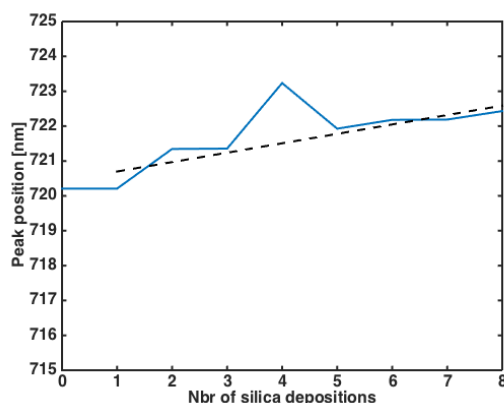


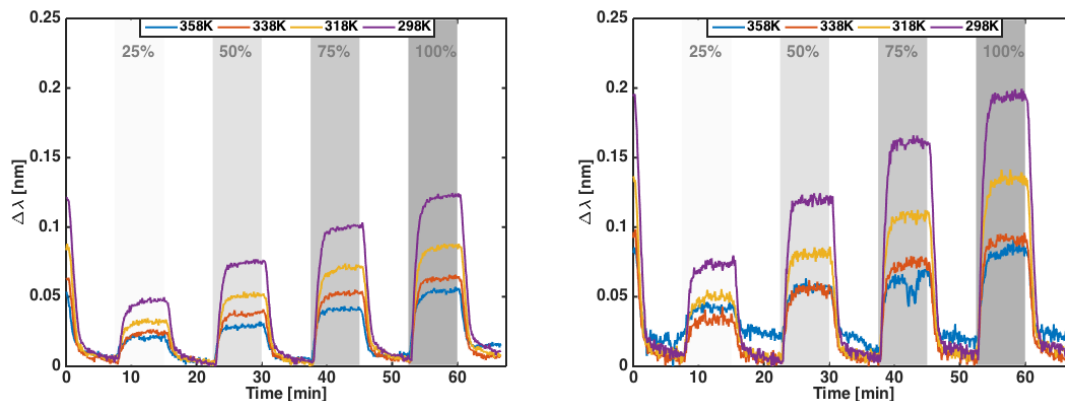
Figure 6.7: The LSPR peak wavelength as a function of the number of silica depositions according to procedure 2 but using the lower concentration of 1wt% instead. The peak red-shifts linearly when adding more silica. The dashed line is a fit to the data excluding the peak after the fourth deposition.

silica nanoparticles of two sizes are studied. One with $130 \text{ m}^2/\text{g}$ specific surface area and average particle diameter of 20 nm and the second with $360 \text{ m}^2/\text{g}$ and average particle diameter of 7 nm. These were deposited following the first and the second procedure, which gave similar results. However, since the effect of the cationic polymer on the LSPR shift is not entirely known, below, the results from measurements on silica deposited by procedure 2 are presented.

As is discussed later on in this section, there exists an uncertainty concerning how to interpret the change of magnitude in LSPR shifts. Therefore, the third deposition procedure was developed from the first two, since none of them provided a way of reproducing reliable LSPR shift magnitudes. Results from measurements of silica deposited by the third procedure are also presented below. There, I believe that I understand the relation between the magnitude of the shifts obtained from the two sizes of NPs.

6.3.1 CO_2 adsorption on silica nanoparticles deposited by procedure 2

In Figures 6.8a and 6.8b, one can see the LSPR shift from CO_2 adsorption on INPS chips with silica NPs deposited by procedure 2 (described in Section 4.3). The second procedure was followed due to uncertainty in how, if at all, the polymer affects the adsorption of CO_2 . For these samples the procedure was repeated 5 times, which has proven to give slightly more than a monolayer of silica particles. There is a significant shift upon CO_2 exposure (grey fields). The adsorption process seems to follow the Langmuir adsorption model, namely the adsorption increases when the CO_2 partial pressure increases. We also see that it decreases for elevated temperatures, which is to be expected since the thermal energy kT is larger than the potential well of the adsorption, thus, the molecules will easily escape from the surface.



(a) 7 nm silica particles, by procedure 2 (b) 20 nm silica particles, by procedure 2

Figure 6.8: LSPR shift for CO₂ adsorption on a sensor with (a) 7 nm and (b) 20 nm silica particles, both deposited by procedure 2. CO₂ exposure of 7.5 minutes each time, at partial pressures 25, 50, 75 and 100% of 1 atm (grey fields) at each temperature; 358 K (blue), 338 K (orange), 318 K (yellow) and 298 K (purple). Note the unexpected relation between $\Delta\lambda$ for the two particles sizes.

Surprising about the results of adsorption on silica NPs deposited by procedure 2 is that the larger particles give a larger LSPR shift compared to the smaller ones. If the sensor surface is covered by equally thick layers, the smaller particles should give rise to a larger LSPR shift, since there is more surface area to adsorb on within the sensing volume of the Au nanodiscs. I believe we see this result because the coverage of the smaller particles is not high enough to yield a larger total surface area within the sensing volume. If one estimates the number of 7 nm particles needed to obtain a larger total surface area than of the 20 nm ones, as the ratio of the squared radii, we have; $20^2/7^2 \approx 8$. Thus, more than 8 small particles are needed to yield a larger total surface area than one large particle. Also by estimation, the coverage of the smaller particles only need to be $7/20 \approx 0.35$ of the coverage of the larger particles to yield more total surface area. As the volume of the larger particles is $20^3/7^3$ times the small particle volume. Which means only one third of the number of large particles is needed of the small particles, thus it seems possible to indeed see the surface area effect.

However, the smaller particles are less prone to be densely packed, because they have a larger tendency to gel than the larger particles. To achieve the same mass concentration of the smaller ones more particles are needed, thus there is less space in between them, which will make them gel at lower concentrations. This could provide an explanation to the larger LSPR shift measured for the 20 nm particles. As the particles on these samples were deposited by procedure 2, in other words, without using the cationic polymer. Perhaps a higher coverage of smaller particles could be obtained by using the cationic polymer in the deposition. Therefore, the third procedure was developed, in an attempt to obtain higher surface coverage.

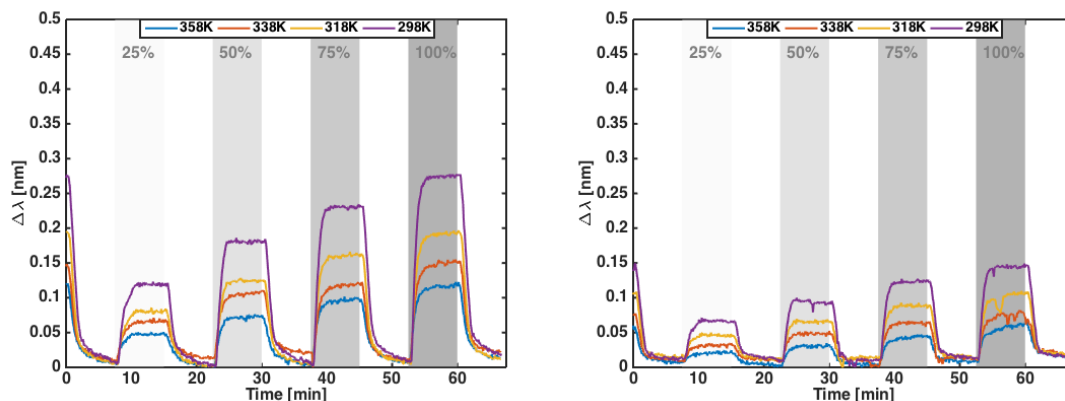
There is also another aspect to be considered, a more densely packed layer gives a higher surrounding RI, which in turn gives a higher sensitivity [20]. It is hard to understand how this affects the sensitivity in this case, as the main part of the volume of the smaller particles is closer to the sensor surface than for the larger particles, it may result in a larger volume close to the surface even though the total volume is much smaller.

6.3.2 CO₂ adsorption on silica nanoparticles deposited by procedure 3

When comparing several measurements, it is further observed that the magnitude of the shifts are not reproducible, also for silica particles modified by amine groups (see Appendix A.5). Even though the samples are prepared in the same way, the LSPR shift magnitude can still vary significantly. As mentioned, it is believed that it can be due to the difference in thickness and density of the silica particle layer on the sensor surface. The reach of the electric field from the gold nanodiscs is not exactly known, but it expands a few tenths of nanometers, including the spacer layer. It is possible to have more than one silica particle on top of each other inside the sensing volume, at least when considering the smaller particles. The LSPR wavelength shift is approximately linearly proportional to the change of RI in the surrounding medium. Thus, it is fair to assume that it is also linearly proportional to the number of CO₂ molecules adsorbed. In this way, the coverage may highly affect the magnitude of the shift, adding more particles will add surface area available for adsorption, until the whole sensing volume is filled up.

To test the hypothesis presented above, a third deposition procedure was developed from the first two. The adsorption measurement on silica particles deposited by this procedure is showed in Figures 6.9a and 6.9b. The expected relation between the magnitude of the shifts is observed, namely, the smaller particles yields a larger LSPR shift. Identical results were obtained for yet another batch of chips with silica NPs deposited by procedure 3 (see Appendix A.4). This indicates that the difference in magnitude of the LSPR shifts, indeed, is due to the coverage on the sensor surface. Which confirms the anticipated relation, that the smaller nanoparticles gives a higher adsorption due to the larger surface area per gram.

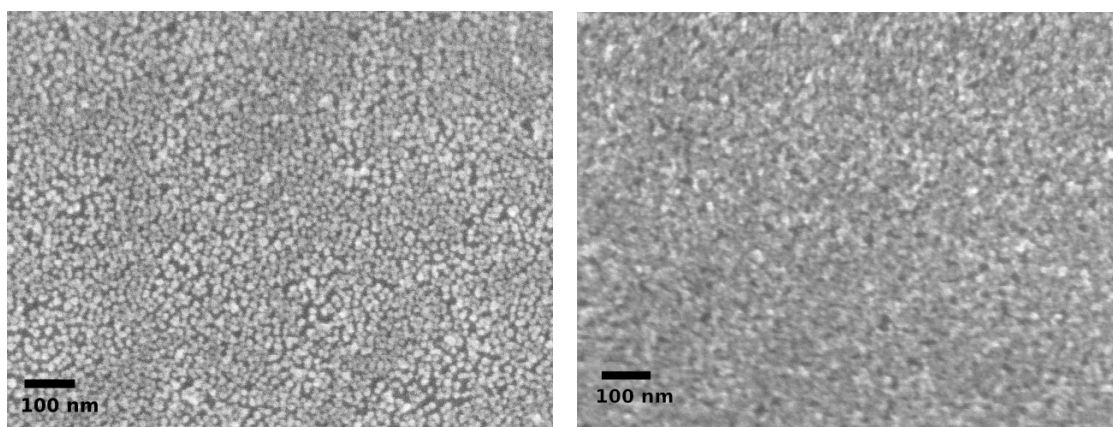
SEM was used to image the coverage on the INPS surfaces, in order to visualize the thicker multilayer obtained by deposition procedure 3. In Figure 6.10a 7 nm silica particles are deposited according to procedure 2, repeated 5 times. It seems to be slightly more than a monolayer covering the Si surface. In Figure 6.10b particles of the same size are deposited according to procedure 3. In the latter case, the layer seems to be thicker and denser. I make this interpretation because it is not possible to distinguish single NPs as in the former image, this assumption is strengthened by imaging a layer deposited identically at 70° inclination (see Appendix C.1). However, the image is not very sharp, when having a thick layer of silica particles the focus is hard to adjust since the surface is uneven. Also, because the layer is thicker and silica is an insulator the surface may be less conductive, which can contribute



(a) 7 nm silica particles, by procedure 3 (b) 20 nm silica particles, by procedure 3

Figure 6.9: LSPR shift for CO₂ adsorption on a sensor with (a) 7 nm and (b) 20 nm silica particles, both deposited by procedure 3. As expected, the smaller particles yield a larger $\Delta\lambda$. CO₂ exposure of 7.5 minutes each time, at partial pressures 25, 50, 75 and 100% of 1 atm (grey fields) at each temperature; 358 K (blue), 338 K (orange), 318 K (yellow) and 298 K (purple).

to the difficulty to focus. However, we can assume that the third procedure results in a much thicker layer.



(a) 7 nm silica particles, by procedure 2 (b) 7 nm silica particles, by procedure 3

Figure 6.10: Si surface covered with 7 nm silica particles deposited either by (a) procedure 2, 5 repetitions or (b) procedure 3. Even though the right image is not sharp, one can see that there is a thicker and denser multi-layer compared to slightly more than a monolayer in the left image.

For imaging by SEM, silica NPs was deposited by procedure 3 on Au nanodiscs fabricated on Si substrates instead of glass and coated by Si₃N₄ analogously to INPS chips, the images are presented in Figure 6.11. We can clearly see that the gold discs are decorated by silica NPs. However, it is troubling that the coverage

is not as high as obtained on Si surfaces. There are enough silica NPs to yield a significant response from the LSPR, but one would wish to have a thicker layer for the consistency and interpretation of the magnitude of the LSPR shift. This behavior might occur because the surface is not as flat as a clean Si substrate, which might complicate the attachment of NPs to the surface. The difference of surface coating, from Si to Si_3N_4 , could also give a slightly less uniform coverage. Silica deposition on Si_3N_4 coated Si has also been studied and did not yield as high coverage as on bare Si substrates (showed in Appendix C.2).

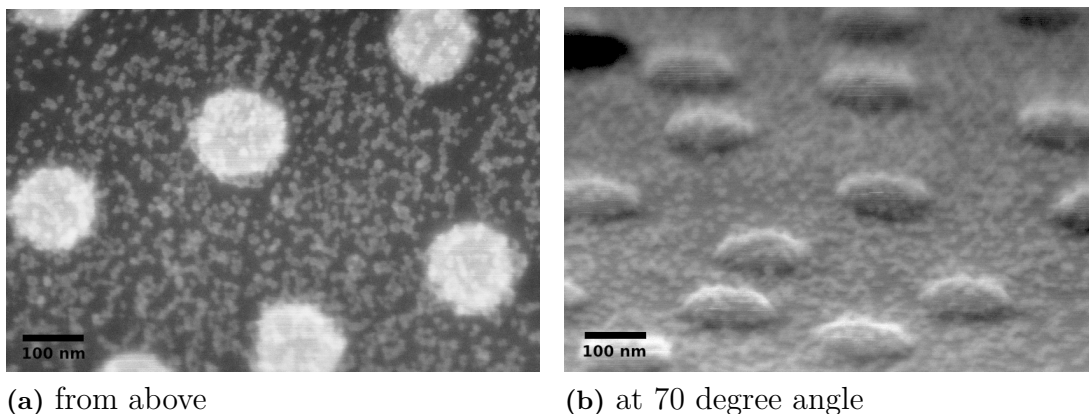


Figure 6.11: INPS chip with 7 nm silica NPs deposited by procedure 3, (a) from above and (b) at 70° angle. We can see silica NPs on top of the gold nanodiscs, however, the coverage is not at all as high as on a Si surface.

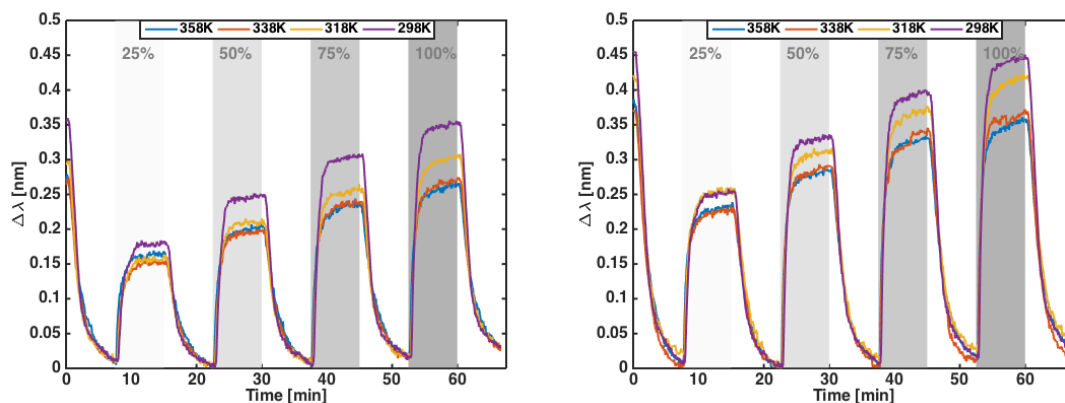
6.4 CO_2 adsorption on silica nanoparticles functionalized by amine groups

One of the main objectives of the thesis work was to investigate if amine functionalization of the silica particles is beneficial for CO_2 adsorption. Identical gas adsorption measurements were performed on the monoamine and triamine functionalized silica particles, as on bare silica particles. In Figures 6.12a and 6.12b, the results of monoamine and triamine silica deposited by procedure 3 are presented. Measurements were also performed with samples prepared following procedure 2. However as discussed previously, no consistent relation between the magnitudes of the shift $\Delta\lambda$ could be noted (see Appendix A.5).

In the results presented here, the response of the triamine functionalized silica is larger compared to the monoamine functionalized. One must keep in mind that the LSPR read-out is unspecific and a difference is introduced between these samples when attaching different molecules on the silica NPs. The triamine contains more amine groups, which increases the RI of the medium surrounding the INPS chip. The electric field is enhanced when increasing the RI, thus, the sensitivity increases. It was showed by Antosiewicz et al [20], that increasing the surrounding RI enhances

the near field of the nanodiscs. As we do not know the density of the amine groups in either of the samples, we cannot conclude how it affects the sensitivity of the enhanced field. Thus, we cannot say if the larger LSPR shift of the triamine sample originates from increased CO_2 adsorption or from enhanced sensitivity. However, we can see that both amine functionalizations do adsorb CO_2 .

If one can assume that the effect of the enhanced field is small in the context, it would mean that the triamine does indeed adsorb more. Which one would expect since there are more amine groups available. However, the response is not tripled, but there are also other factors governing the amount of adsorbed CO_2 . If one speculates, one possible reason could be that the triamine carbon chain has a larger volume, thus, there is less room for triamine molecules, which means that the actual number of amine groups is not tripled. Another possible explanation could be that the amine carbon chains do not cover the entire silica surface area. Thus, the CO_2 still has the possibility of binding directly to the silica surface, as has been seen for the bare silica samples. To conclude anything from these speculations, one needs more knowledge about the amine molecules and how they cover the silica nanoparticle surface.



(a) 7 nm silica particles with monoamine (b) 7 nm silica particles with triamine

Figure 6.12: LSPR shift for CO_2 adsorption on 7 nm silica functionalized by (a) monoamines and (b) triamines, in both cases deposited by procedure 3. CO_2 exposure of 7.5 minutes each time, at partial pressures 25, 50, 75 and 100% of 1 atm (grey fields) at each temperature; 358 K (blue), 338 K (orange), 318 K (yellow) and 298 K (purple).

For this measurement, the same scheme was followed for running the X1 gas reactor as before. When comparing the shape of the adsorption diagram for the amine functionalized silica particles in Figures 6.12a and 6.12b with the bare silica particles in Figures 6.9a and 6.9b, one finds an interesting difference. In the amine functionalized case, we observe that the adsorption does not reach a steady state before desorbing CO_2 after 7.5 minutes. To try and reach a steady state, a 40 hours long adsorption and desorption run was done (20 hours adsorption with and

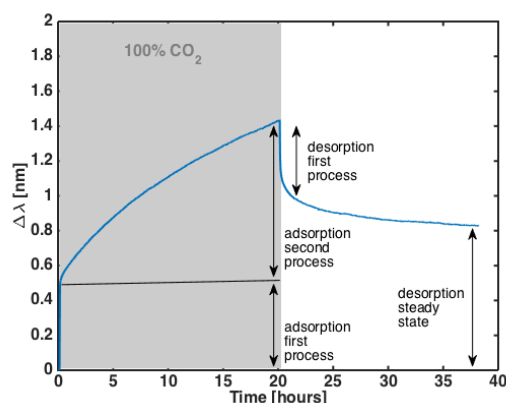


Figure 6.13: Longer CO₂ adsorption run at 298 K in X1 gas setup. Adsorption measured during 20 hours followed by desorption for 20 hours. It is obvious that the steady state for the adsorption is not yet reach after 20 hours, however, desorption seems to level out at 0.8. The LSPR red-shifts caused by the two different processes are marked as well as the desorption steady state.

desorption intervals, respectively). The corresponding LSPR shifts are presented in Figure 6.13. This measurement was performed at 298 K and 100% CO₂, which has proven to give the highest adsorption, but first the sample was heated at 358 K for 2 hours to evaporate possible solvent residuals. It is obvious that so far a steady state is not reached for the CO₂ adsorption, whereas the desorption seems to level out around $\Delta\lambda = 0.8$. Thus, it does never return to the original level seen before the adsorption interval. This is indeed an interesting finding, it may indicate that there is a second process going on, which takes far longer time than the first one, which causes the fast LSPR change.

If I may speculate, this second process might be chemisorption of CO₂. Others have reported on measuring chemisorbed CO₂ on amine functionalized silica. Danon et al [12], did find that CO₂ formed surface bound carbamates (explained in Chapter 2). These surface-bound carbamates did not evacuate at room temperature, which correlates well with the findings of this thesis. When studying Figure 6.13 more closely, one can note that the first process yields a red-shift of approximately 0.5 nm and the second slower process yields a shift of almost 1 nm, marked in the figure. If one were to assume that the chemisorbed CO₂ does not evacuate at room temperature, the 1 nm shift caused by the second process is exactly what the desorption levels out at. Since, chemisorbed CO₂ does not evacuate, it remains on the sensor surface and still causes $\Delta\lambda \approx 1$ nm after 20 hours. However, these are only speculations so far and need to be investigated further before making any final conclusions, but it is indeed an interesting finding.

6.5 Average isosteric heat of adsorption

One important aspect of optimizing a carbon dioxide capturing system is to find a material that gives a suitable isosteric heat of adsorption of CO₂ Q_{st} . The enthalpic gain of adsorbing CO₂, thus, the isosteric heat at the operating temperature needs to be high enough for adsorption to happen. On the other hand, if the binding energy is high, desorbing CO₂ from the system will require a lot of energy, which of course is unfavorable. Thus, determining the isosteric heat of CO₂ adsorption is vital. By fitting the maximum $\Delta\lambda$ at each partial pressure of CO₂ to the Langmuir adsorption model for all temperatures and fitting the obtained parameters to the Van't Hoff eq. (3.8), one can estimate the isosteric heat of adsorption as explained in Section 3.2. As $\Delta\lambda$ is taken from the first adsorption process and not the second slower process observed in the previous section, it is the enthalpic change associated with physisorption that is calculated here.

Both parameters Γ_∞ and K in the Langmuir model eq. (3.6), are fitted from experimental data. Maximum coverage Γ_∞ is assumed to be directly proportional to the maximum shift of all temperatures. It is usually found at 298 K and assumed to be identical at all temperatures. It makes sense because the number of sites does not change but the probability for adsorption goes down when temperature increases. In Figures 6.14a and 6.14b, we can see two examples of the parameters obtained from the Langmuir fit, these are for bare silica NPs deposited by procedure 3 (the shift is seen in Figures 6.9a and 6.9b). The logarithm of the equilibrium constants K at each temperature are plotted against the inverse temperature. As we can see the relation is relatively linear. The isosteric heat is obtained as the negative slope of the fitted line, according to the Van't Hoff equation. The linear fit of the parameters from other measurements can be found in Appendix B.2.

To get an overview, the average isosteric heats of adsorption of CO₂ for the four systems tested are presented in Figure 6.15. The average isosteric heat of bare silica NPs of both sizes, is almost 20 kJ/mol, the average for 20 nm and 7 nm NPs are 19.5 kJ/mol and 20.2 kJ/mol, respectively. As only the size differs between them, it is to be expected that they have similar isosteric heats. These are all reasonable values for physisorbed CO₂. Belmabkhout et al [21] measured the isosteric heat of CO₂ adsorption on mesoporous silica to be 21.6 kJ/mol. The amine functionalized silica has a slightly lower average at 14.6 kJ/mol, as seen in the figure. The averages of respective functionalization lies close to the total average, with the monoamine functionalized at 14.8 kJ/mol and triamine at 14.4 kJ/mol. The average of 20 nm NPs are taken over 5 measurements, whereas the others over 3. Excluded from the averages, however, are the energies of amine functionalized silica deposited by procedure 3 i.e. the LSPR shifts presented in Figures 6.12a and 6.12b. These values were significantly lower than the others, however, still within the limit for what is reasonable. The isosteric heat for monoamine and triamine functionalization was estimated to $Q_{st} = 7.9$ kJ/mol and $Q_{st} = 7.0$ kJ/mol, respectively. For bare silica particles however, both isosteric heats from samples prepared by procedure 2 and 3 are included in the averages, for the 20 nm NPs also one sample by procedure 1 is

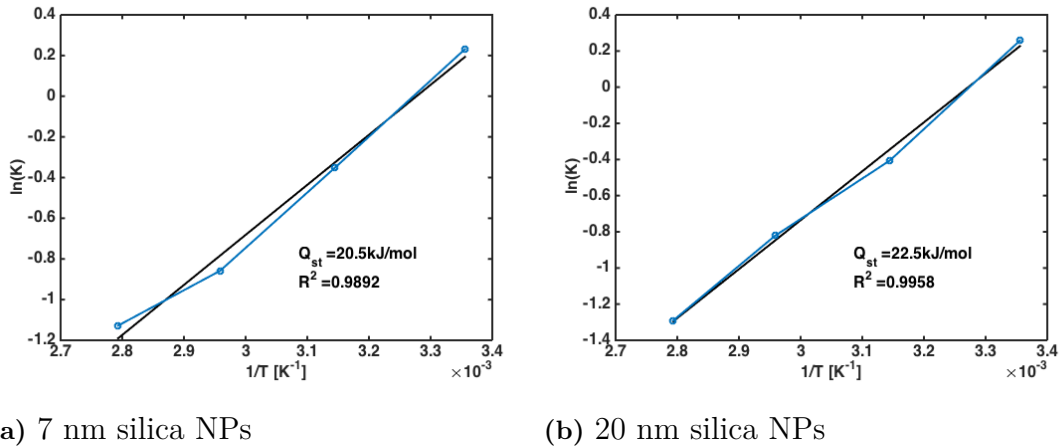


Figure 6.14: The parameters from fitting the data to the Langmuir adsorption model for (a) 7 nm and (b) 20 nm silica NPs, deposited by procedure 3. $\ln(K)$ is plotted as function of T^{-1} , according to the Van't Hoff equation the enthalpic change i.e. the negative isosteric heat, is the slope of the line. The black line is the linear fit.

included.

In literature, the isosteric heats of adsorption of CO_2 on silica functionalized by amines have been reported to vary with the amine loading, whereas for bare silica systems it seems to stay rather constant. Belmabkhout et al [21] have measured the isosteric heat of CO_2 adsorbed on the commercially available mesoporous silica structure MCM-41. They found that it varied between 22 – 19 kJ/mol depending on the amount of adsorbed CO_2 , where the lower isosteric heat corresponds to higher CO_2 loading. Thus, there is a small variation in the isosteric heat for the bare silica system, which agrees with what I have observed. There is no significant difference between the isosteric heats calculated from samples prepared by procedures 2 and 3. The values they have found also agrees with my results. Belmabkhout et al have also measured the isosteric heat of triamine functionalized mesoporous silica and found that it decreases drastically with the CO_2 loading [22]. At low CO_2 loadings (1 mmol/g), Q_{st} can be as high as 90 kJ/mol, whereas, at higher loadings Q_{st} approaches 10 kJ/mol. Thus, they saw a completely different behavior for the amine functionalized silica system compared to the bare silica structure. This can explain why I have found lower Q_{st} for the samples prepared by procedure 3. Since these samples show larger LSPR shifts one can assume that there is more CO_2 adsorbed, which, according to Belmabkhout, should yield lower Q_{st} .

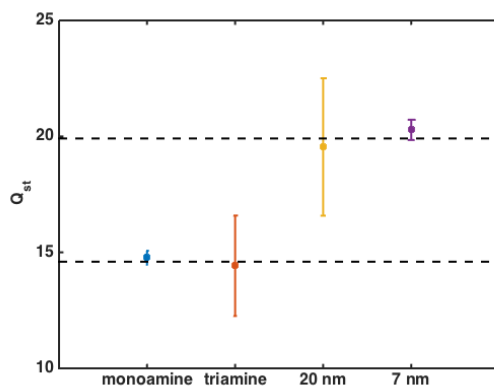


Figure 6.15: The average isosteric heat of adsorption for each of the four systems studied, from the left; 7 nm silica NPs with monoamines, with triamines, bare 20 nm silica NPs and bare 7 nm silica NPs. The errorbars are taken as the maximum deviation from the average of measurements. For the 20 nm the average is taken over 5 measurements, for the remaining cases the average is over 3 measurements. The dashed lines are the average isosteric heat of bare silica NPs (the upper line) and silica NPs functionalized with amines (the lower line).

7

Conclusion and outlook

The thesis aims to investigate the possibilities of using colloidal silica particles for CCS purposes and the INPS platform as experimental method to investigate the adsorption process. It has been shown that INPS is possible to use for detecting adsorption of CO₂, as has also previously been done by Nugroho et al for a microporous polymer CO₂ sorbent [8]. The measured LSPR changes were distinct and no uncertainty in the origin of the shift existed. The magnitude of the shift decreases unambiguously with temperature in all measured cases, which indicates that we are indeed measuring adsorption of CO₂. Thus, it is clear that silica particles can be used for CO₂ adsorption.

The surface area of the sorption material affects the amount of adsorbed CO₂ within the sensing volume of the LSPR sensors, as one would expect. This was established by depositing silica NPs by procedure 3, which was developed from the to original procedures to yield a thicker layer of silica NPs. A comparison of the magnitude of the shifts for both particles sizes indicated that the smaller particles indeed adsorbed more CO₂ in the sensing volume due to the larger surface area within the sensing volume. By following the third procedure it was possible to produce this expected relation of the magnitudes of the LSPR shifts of the bare silica samples. This was the most critical and difficult part of the preparation. I believe it is necessary to use a cationic polymer to obtain a thick layer of silica. To yield an even thicker layer than what was achieved with procedure 3, for even more durability and reliability, one could try using higher polymer concentration. The surface area of the smaller particles was 360 m²/g, which, compared to materials engineered to have an extremely high surface area, is not very much. One can find materials with over 1000 m²/g. AkzoNobel PPC AB for example provides one high specific surface area product with 1100 m²/g. To enhance the efficiency of the sorption material, one could in the future investigate the possibilities of functionalizing such materials.

In order to achieve higher CO₂ selectivity, silica NPs functionalized by amine carbon chains were studied. The environment surrounding the INPS chips was changed both between the monoamine and the triamine functionalized silica, but also compared to the bare silica NPs. Thus, it is not possible to compare the magnitude of the shifts, since the increase in RI may enhance the near field of the nanodiscs. However, we can note that for both amine functionalizations and particularly the triamine case, there is a large change in LSPR. This is indeed interesting results, but need further investigations to draw any conclusions of which functionalization is most efficient. To measure the amount of adsorbed CO₂ QCM would be a suitable

method to use, since one can monitor the amount of adsorbed CO_2 on the silica system.

It is proven that LSPR and in particular the INPS platform, provides a convenient method of monitoring the process of exposing the bare silica and amine functionalized silica to CO_2 . One can not conclude anything about the absolute amounts of adsorbed CO_2 . However, it is possible to study the adsorption process as well as the kinetics, to identify the different processes taking place, such as the assumed chemisorption in this work. With further knowledge about the amine density on the silica surface, one could probably establish a formula for the enhancement of the sensitivity due to the increased RI of the surrounding by using results from previous studies, such as the one by Antosiewicz et al [20]. Thus, eliminating the effect of the enhanced sensitivity and making it possible to directly compare the magnitude of the LSPR shifts and conclude which system is more efficient for CO_2 adsorption.

It was also found that the behavior of the LSPR response was different for silica NPs modified by amines compared to bare silica NPs. Both adsorption and desorption needs longer time to reach equilibrium. Still after 20 hours, there was no sign of reaching a steady state for the adsorption, the desorption however, had leveled out. This is discussed more thoroughly in Section 6.4, where the possibility of a second process, which could be chemisorption, is mentioned. This is a very intriguing discovery indeed, as chemisorption together with physisorption has been observed in several other works. Thus, it is reasonable to assume it could be an explanation for the behavior observed in my work. Of course, further investigation is needed to draw any conclusions, hence, the temperature dependence of the assumed chemisorbed species is yet another possibility for future studies. It would, along with IR spectroscopy which is an established method for monitoring bonds, provide an appropriate method for distinguishing between physisorbed and chemisorbed CO_2 .

Collected adsorption kinetic data correlate well with the Langmuir adsorption model, which was used as one step in the estimation of the isosteric heat of adsorption. The values obtained, around 10 – 20 kJ/mol, were well within what is reasonable and agrees with other values found in literature. Of particular interest was the work of Belmabkhout et al [22], who have found that the isosteric heat of CO_2 adsorption on triamines decreases when more CO_2 adsorbs. We have also seen a possible indication of decrease in isosteric heat in this work. The absolute largest LSPR shifts, namely from triamine and monoamine functionalized NPs deposited by procedure 3, corresponded to a significantly lower isosteric heat than the other samples. This was only measured once and no rigorous conclusions can be drawn from this, but it may be something to investigate further in future studies, as it does indeed suggest an interesting behavior.

For better comparison with other studies one should consider measuring the adsorbed CO_2 in the relation to the total amount of the sorbent material, as this is a very important aspect when considering the efficiency of the sorbent. Exact quantitative measurements of amounts of adsorbed gas are difficult with LSPR, one need

some reference to absolutely correlated the magnitude of the shift with the adsorbed amount. Instead, QCM might be more suitable to use, which works more like a scale, when mass is adsorbed on the QCM surface the resonance frequency of the quartz crystal changes. As the mass of one carbon dioxide molecule is known, it should be possible to calculate the exact amount of adsorbed CO₂ molecules and express as g-CO₂/g-sorbent. However, this requires the exact amount of silica coverage on the QCM sensor to be known.

To summarize, amine functionalized silica NPs show suitable properties to be used as sorbent material for CO₂ in CCS techniques. Silica functionalized by triamines showed higher adsorption compared to monoamine functionalized. The isosteric heats calculated were all within reason and comparable to the literature. There are several possibilities for future investigations, among them, determine if CO₂ also is chemisorbed, engineering the amine carbon chains for higher adsorption or measure the absolute amount of adsorbed CO₂ per amount sorbent material.

Bibliography

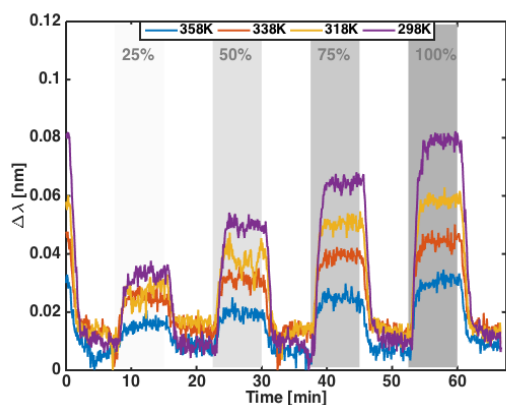
- [1] Howard Herzog and Dan Golomb. “Carbon Capture and Storage from Fossil Fuel Use”. In: *Encyclopedia of Energy* 1 (2004).
- [2] Francesc Sastre et al. “Complete Photocatalytic Reduction of CO₂ to Methane by H₂ under Solar Light Irradiation”. In: *Journal of the American Chemical Society* 136.19 (2014), pp. 6798–6801.
- [3] Yuanyuan Liu et al. “Selective ethanol formation from photocatalytic reduction of carbon dioxide in water with BiOV₄ photocatalyst”. In: *Catalysis Communications* 11.3 (2009), pp. 210–213.
- [4] Bert Metz et al. *IPCC Special Report on Carbon Dioxide Capture and Storage*. Cambridge University Press. 2005.
- [5] Global CCS Institute. *The Global Status of CCS: 2014*. Melbourne, Australia. 2014.
- [6] A. L. Myers. “Thermodynamics of Adsorption in Porous Materials”. In: *Thermodynamics* 48.1 (2002).
- [7] Christoph Langhammer et al. “Indirect Nanoplasmonic Sensing: Ultrasensitive Experimental Platform for Nanomaterials Science and Optical Nanocalorimetry”. In: *Nano Letters* 10.9 (2010), pp. 3529–3538.
- [8] Ferry A. A. Nugroho et al. “UV–Visible and Plasmonic Nanospectroscopy of the CO₂ Adsorption Energetics in a Microporous Polymer”. In: *Analytical Chemistry* 87.20 (2015), pp. 10161–10165.
- [9] Chungsyng Lu et al. “Adsorption of Carbon Dioxide from Gas Streams via Mesoporous Spherical-Silica Particles”. In: *Journal of the Air & Waste Management Association* 60.4 (2010), pp. 489–496.
- [10] T. Sakpal et al. “Carbon dioxide capture using amine functionalized silica gel”. In: *Indian Journal of chemistry* 51A (Sept. 2012), pp. 1214–1222.
- [11] Zhonghua Zhang et al. “Development of silica-gel-supported polyethylenimine sorbents for CO₂ capture from flue gas”. In: *AIChE Journal* 58.8 (2012), pp. 2495–2502.
- [12] Alon Danon, Peter C. Stair, and Eric Weitz. “FTIR Study of CO₂ Adsorption on Amine-Grafted SBA-15: Elucidation of Adsorbed Species”. In: *The Journal of Physical Chemistry C* 115.23 (2011), pp. 11540–11549.
- [13] Zoltán Bacsik et al. “Temperature-Induced Uptake of CO₂ and Formation of Carbamates in Mesocaged Silica Modified with n-Propylamines”. In: *Langmuir* 26.12 (2010), pp. 10013–10024.
- [14] Nicholas A. Brunelli et al. “Tuning Cooperativity by Controlling the Linker Length of Silica-Supported Amines in Catalysis and CO₂ Capture”. In: *Journal of the American Chemical Society* 134.34 (2012), pp. 13950–13953.

- [15] Horacio E Bergna. “Colloid Chemistry of Silica”. In: *Colloidal Silica*. CRC Press, 2015/10/07 2005, pp. 9–35.
- [16] Kurt K. Kolasinski. *Surface Science: Foundation of Catalysis and Nanoscience*. 3rd. John Wiley, 2012.
- [17] Ferry A. A. Nugroho. “Nanoplasmonic Sensing of Materials for Energy Applications”. PhD thesis. Chalmers University of Technology, 2016.
- [18] H. Fredriksson et al. “Hole–Mask Colloidal Lithography”. In: *Advanced Materials* 19.23 (2007), pp. 4297–4302.
- [19] You-Ting Wu et al. “Quartz Crystal Microbalance (QCM) in High-Pressure Carbon Dioxide (CO₂): Experimental Aspects of QCM Theory and CO₂ Adsorption”. In: *Langmuir* 20.9 (2004), pp. 3665–3673.
- [20] Tomasz J. Antosiewicz, Carl Wadell, and Christoph Langhammer. “Plasmon-Assisted Indirect Light Absorption Engineering in Small Transition Metal Catalyst Nanoparticles”. In: *Advanced Optical Materials* 3.11 (2015), pp. 1591–1599.
- [21] Youssef Belmabkhout, Rodrigo Serna-Guerrero, and Abdelhamid Sayari. “Adsorption of CO₂ from dry gases on MCM-41 silica at ambient temperature and high pressure”. In: *Chem. Eng. Science* 64.17 (2009), pp. 3721–3728.
- [22] Youssef Belmabkhout and Abdelhamid Sayari. “Effect of pore expansion and amine functionalization of mesoporous silica on CO₂ adsorption over a wide range of conditions”. In: *Adsorption* 15.3 (2009), pp. 318–328.

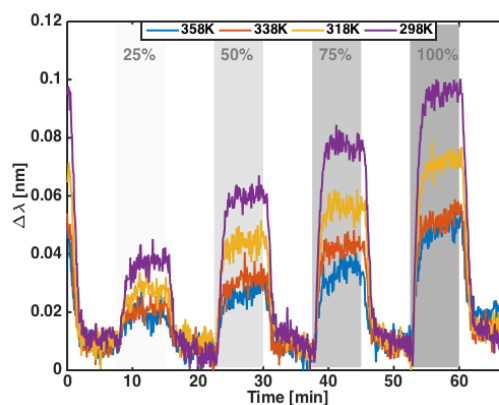
A

Appendix 1

A.1 170 nm Au nanodiscs



(a) 140 nm Au disc



(b) 170 nm Au disc

Figure A.1: LSPR wavelength shift of an INPS chip with Au discs of diameter (a) 140 nm and (b) 170 nm, covered with silica NPs deposited by procedure 1. There is no significant difference in the LSPR response, the magnitude of the shifts are comparable, and as discussed previously not reliable from procedure 1 or 2. CO₂ partial pressures 25, 50, 75 and 100% (grey fields) at temperatures 358 K (blue), 338 K (orange), 318 K (yellow) and 298 K (purple).

A.2 Control measurement of adsorption on polymer

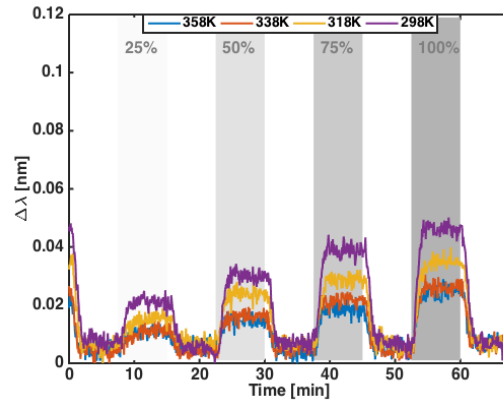
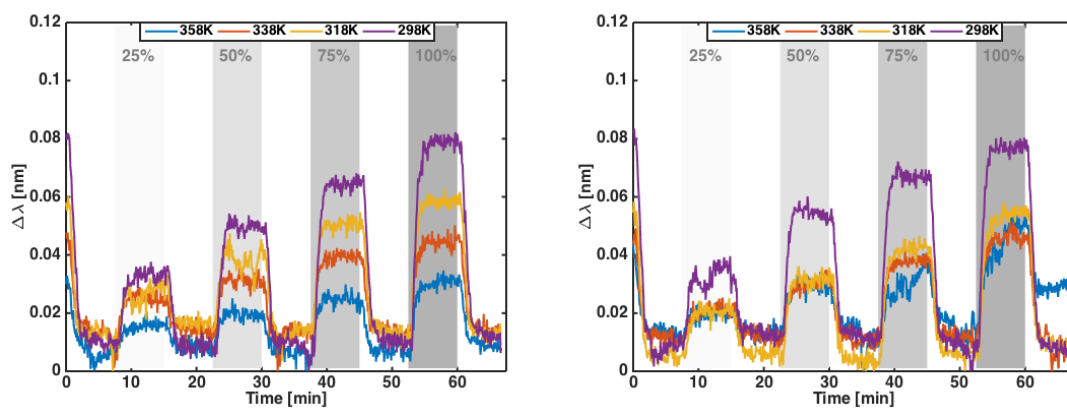


Figure A.2: LSPR wavelength shift of an INPS chip with cationic polymer drop-coated for 2 minutes. CO₂ partial pressures 25, 50, 75 and 100% (grey fields) at temperatures 358 K (blue), 338 K (orange), 318 K (yellow) and 298 K (purple).

A.3 Silica NPs deposited by procedure 1 and 2



(a) 20 nm by procedure 1

(b) 20 nm by procedure 2

Figure A.3: LSPR wavelength shift of an INPS chip with 20 nm silica NPs deposited by (a) procedure 1 and (b) procedure 2. CO₂ partial pressures 25, 50, 75 and 100% (grey fields) at temperatures 358 K (blue), 338 K (orange), 318 K (yellow) and 298 K (purple).

A.4 Control measurement of silica NPs deposited by procedure 3

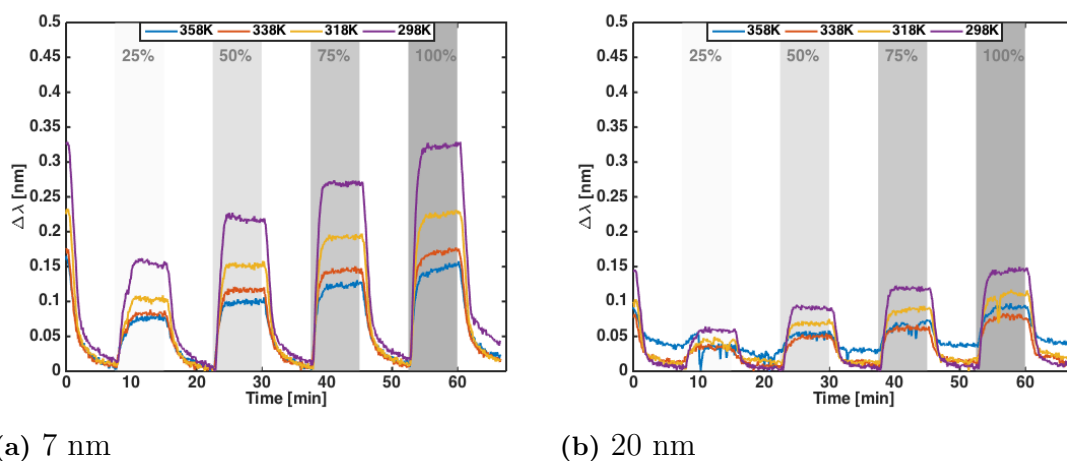
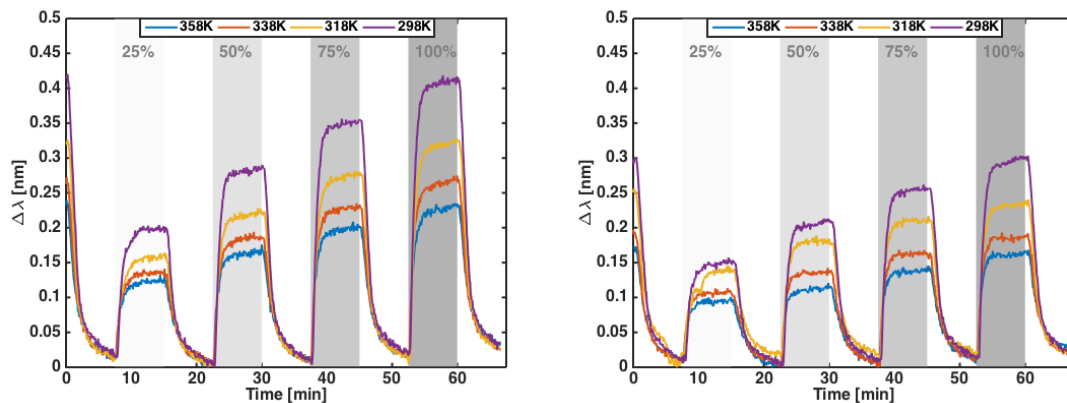


Figure A.4: LSPR wavelength shift of an INPS chip with (a) 7 nm NPs and (b) 20 nm NPs deposited by procedure 3. CO₂ partial pressures 25, 50, 75 and 100% (grey fields) at temperatures 358 K (blue), 338 K (orange), 318 K (yellow) and 298 K (purple).

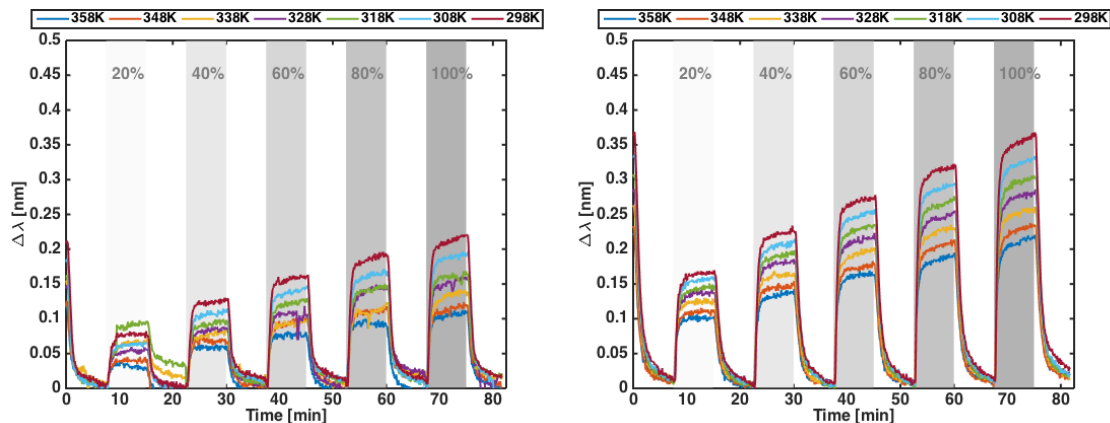
A.5 Amine functionalized silica NPs deposited by procedure 2



(a) monoamine, 1st sample

(b) triamine, 1st sample

Figure A.5: LSPR wavelength shift of an INPS chip with (a) monoamine functionalized 7 nm NPs and (b) triamine functionalized, all deposited by procedure 2. CO₂ partial pressures 25, 50, 75 and 100% (grey fields) at temperatures 358 K (blue), 338 K (orange), 318 K (yellow) and 298 K (purple). Note that in this case, the monoamine has the largest shifts.



(a) monoamine, 2nd sample

(b) triamine, 2nd sample

Figure A.6: LSPR wavelength shift of an INPS chip with (a) monoamine functionalized 7 nm NPs and (b) triamine functionalized, all deposited by procedure 2. CO₂ partial pressures 20, 40, 60, 80 and 100% (grey fields) at temperatures 358 K (blue), 348 K (orange), 338 K (yellow), 328 K (purple), 318 K (green), 308 K (light-blue) and 298 K (red). Note that in this case, the triamine has the largest shifts, oppositely to the previous samples. These are not the same samples as above, but from the same batch of INPS chips.

B

Appendix 2

B.1 Langmuir model fit parameters

Table B.1: The parameters obtained from the Langmuir fitting of the data from the CO₂ adsorption measurement of bare 20 nm silica NPs deposited by procedure 1 and 2 respectively, LSPR response in Appendix A.3.

	20 nm NPs by procedure 1			20 nm NPs by procedure 2		
Temp. [K]	Q_{max}	K	R^2	Q_{max}	K	R^2
298	0.1589	0.9321	0.9961	0.1546	1.0493	0.9940
318	0.1589	0.5616	0.8495	0.1546	0.5713	0.9896
338	0.1589	0.3874	0.7487	0.1546	0.4143	0.9922
358	0.1589	0.2498	0.9322	0.1546	0.3254	0.9835

Table B.2: The parameters obtained from the Langmuir fitting of the data from the CO₂ adsorption measurement of bare 7 nm and 20 nm silica NPs deposited by procedure 2, LSPR response in Figures 6.8a and 6.8b.

	7 nm NPs by procedure 2			20 nm NPs by procedure 2		
Temp. [K]	Q_{max}	K	R^2	Q_{max}	K	R^2
298	0.2627	0.8567	0.9989	0.4669	0.7352	0.9989
318	0.2627	0.5108	0.9971	0.4669	0.4282	0.9971
338	0.2627	0.3358	0.9863	0.4669	0.2798	0.9863
358	0.2627	0.2100	0.9901	0.4669	0.2100	0.9901

Table B.3: The parameters obtained from the Langmuir fitting of the data from the CO₂ adsorption measurement of bare 7 nm and 20 nm silica NPs deposited by procedure 3, LSPR response in Figures 6.9a and 6.9b.

	7 nm NPs by procedure 3			20 nm NPs by procedure 3		
Temp. [K]	Q_{max}	K	R^2	Q_{max}	K	R^2
298	0.4842	1.2603	0.9994	0.2461	1.2940	0.9994
318	0.4842	0.7032	0.9922	0.2461	0.6665	0.9922
338	0.4842	0.4239	0.9462	0.2461	0.4397	0.9462
358	0.4842	0.3238	0.9894	0.2461	0.2750	0.9894

Table B.4: The parameters obtained from the Langmuir fitting of the data from the control measurement of CO₂ adsorption on bare 7 nm and 20 nm silica NPs deposited by procedure 3, LSPR response in Appendix A.4.

	7 nm NPs by procedure 3			20 nm NPs by procedure 3		
Temp. [K]	Q_{max}	K	R^2	Q_{max}	K	R^2
298	0.4782	1.7606	0.9973	0.2925	1.0012	0.9973
318	0.4782	0.9414	0.9933	0.2925	0.5517	0.9933
338	0.4782	0.6215	0.9701	0.2925	0.3760	0.9701
358	0.4782	0.4596	0.9453	0.2925	0.2499	0.9453

Table B.5: The parameters obtained from the Langmuir fitting of the data from the measurement of amine modified silica deposited by procedure 2, the first samples, LSPR response in Figure A.5.

	Monoamine			Triamine		
Temp. [K]	Q_{max}	K	R^2	Q_{max}	K	R^2
298	0.6320	1.7199	0.9996	0.4248	2.1347	0.9987
318	0.6320	1.1240	0.9897	0.4248	1.4258	0.9263
338	0.6320	0.8026	0.9735	0.4248	0.9343	0.9427
358	0.6320	0.6378	0.9325	0.4248	0.7086	0.9209

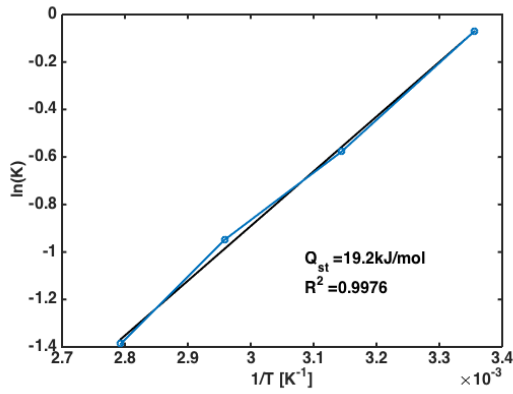
Table B.6: The parameters obtained from the Langmuir fitting of the data from the measurement of amine modified silica deposited by procedure 2, the second samples, LSPR response in Figure A.6.

Temp. [K]	Monoamine			Triamine		
	Q_{max}	K	R^2	Q_{max}	K	R^2
298	0.3980	1.2162	0.9988	0.5115	2.1209	0.9961
308	0.3980	0.9761	0.9993	0.5115	1.7708	0.9941
318	0.3980	0.8232	0.8930	0.5115	1.5244	0.9844
328	0.3980	0.7208	0.9918	0.5115	1.3011	0.9726
338	0.3980	0.5960	0.9231	0.5115	1.1040	0.9746
348	0.3980	0.5176	0.9752	0.5115	0.9409	0.9664
358	0.3980	0.4237	0.9856	0.5115	0.7872	0.9503

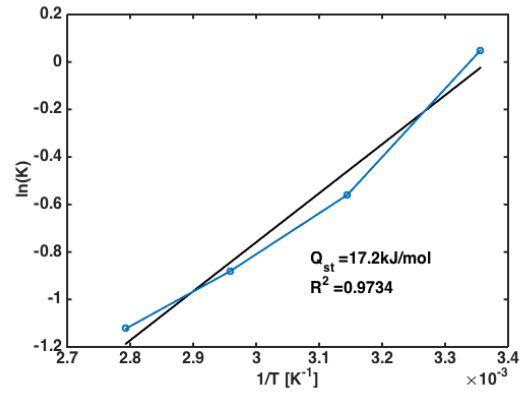
Table B.7: The parameters obtained from the Langmuir fitting of the data from the measurement of amine modified silica deposited by procedure 3 yielding a thicker layer, LSPR response in Figures 6.12a and 6.12b.

Temp. [K]	Monoamine			Triamine		
	Q_{max}	K	R^2	Q_{max}	K	R^2
298	0.5151	1.9491	0.9991	0.5683	3.0966	0.9985
318	0.5151	1.3998	0.9927	0.5683	2.5689	0.9940
338	0.5151	1.1861	0.9664	0.5683	2.2156	0.9793
358	0.5151	1.1469	0.9267	0.5683	1.9269	0.9630

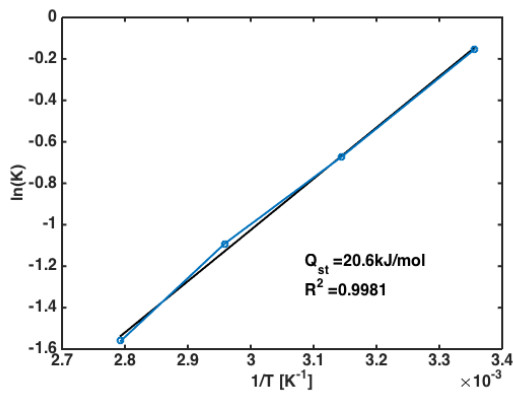
B.2 Isothermic heats from all measurements



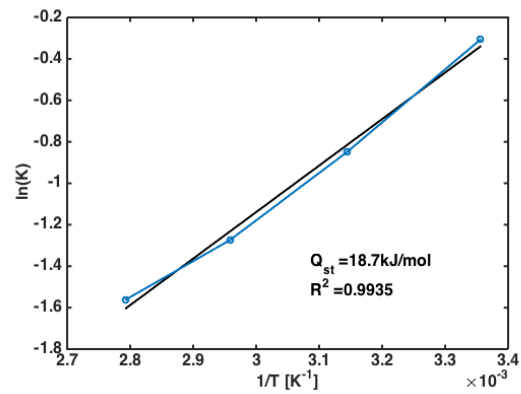
(a) 20 nm by procedure 1



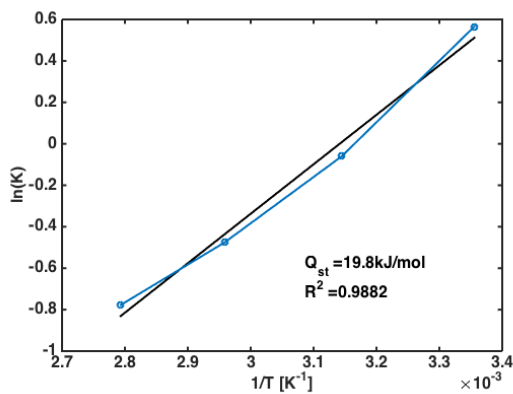
(b) 20 nm by procedure 2



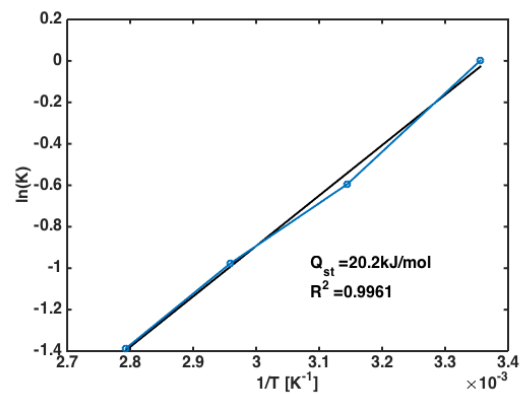
(c) 7 nm by procedure 2



(d) 20 nm by procedure 2

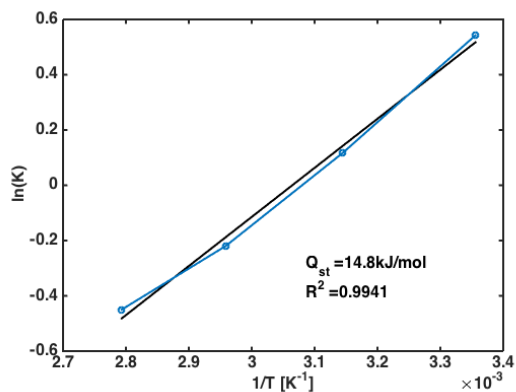


(e) 7 nm by procedure 3, 2nd sample

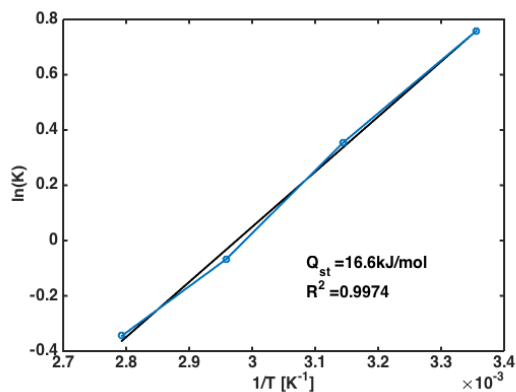


(f) 20 nm by procedure 3, 2nd sample

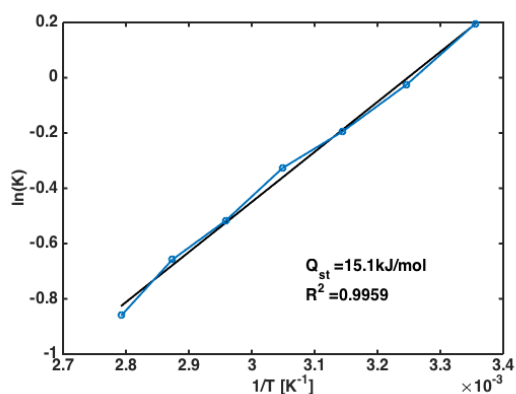
Figure B.1: Linear fit of parameters from Langmuir adsorption model (presented in Tables B.1, B.2 and B.4), the isosteric heat is found as the slope of the line. 20 nm silica NPs by (a) procedure 1 and (b) procedure 2 (LSPR response in Appendix A.3), (c) 7 nm NPs and (d) 20 nm NPs, both deposited by procedure 2 (LSPR response in Figures 6.8a and 6.8b), (e) 7 nm and (f) 20 nm NPs, control measurement by procedure 3 (LSPR response in Appendix A.4). IX



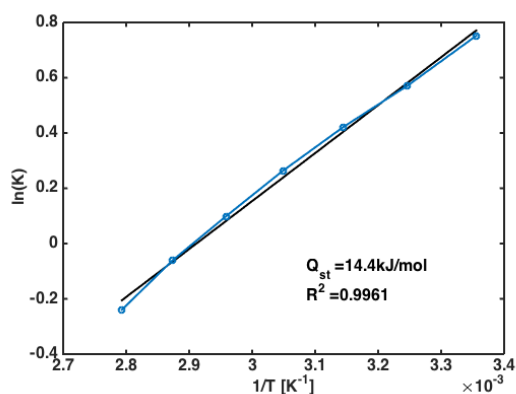
(a) monoamine, 1st samples



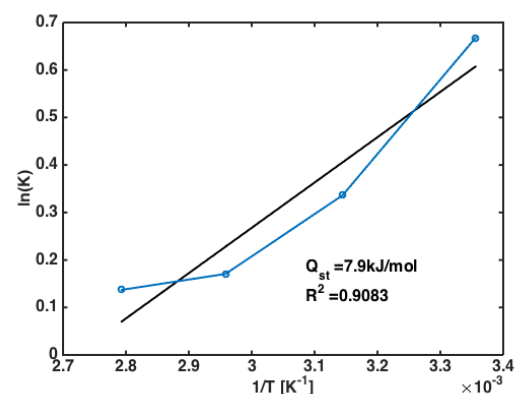
(b) triamine, 1st samples



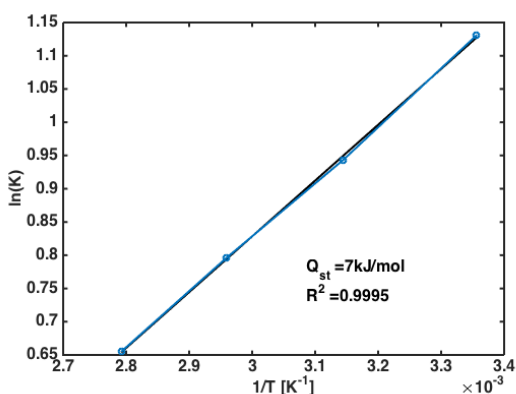
(c) monoamine, 2nd samples



(d) triamine, 2nd samples



(e) monoamine by procedure 3



(f) triamine by procedure 3

Figure B.2: Linear fit of parameters from Langmuir adsorption model (presented in Tables B.5 to B.7), the isosteric heat is found as the slope of the line. First samples of (a) monoamine and (b) triamine functionalization deposited by procedure 2 (LSPR response in Figure A.5), second sample of (c) monoamine and (d) triamine functionalization, deposited by procedure 2 (LSPR response in Figure A.6), (e) monoamine and (f) triamine, deposited by procedure 3 (LSPR response in Figures 6.12a and 6.12b).

C

Appendix 3

C.1 7 nm silica NPs imaged at 70 degree angle

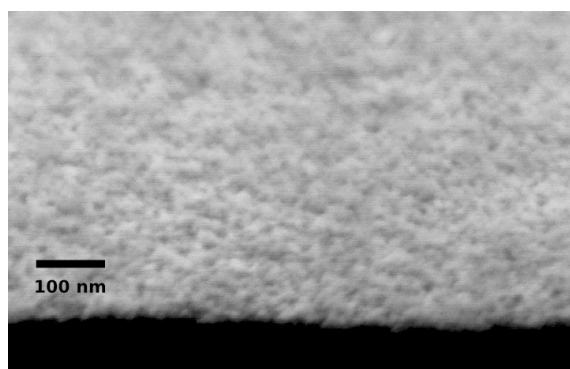
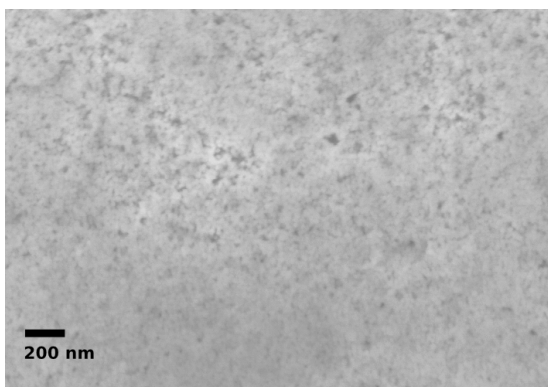
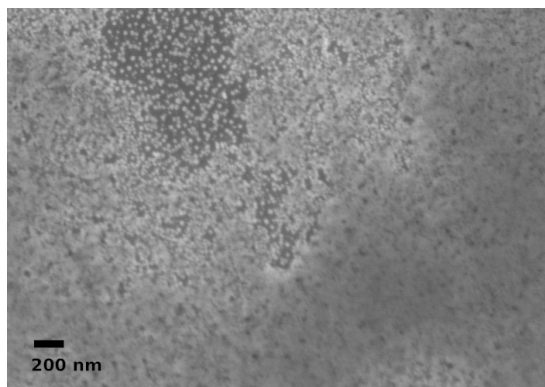


Figure C.1: 7 nm silica NPs deposited by procedure 3, imaged at 70° angle. One can see that it is indeed a thick layer.

C.2 20 nm silica NPs on Si₃N₄



(a) 20 nm on Si



(b) 20 nm on Si₃N₄

Figure C.2: 20 nm silica NPs deposited by procedure 1 on (a) Si wafers and (b) Si wafers coated by 10 nm Si₃N₄. In (a) a fairly thick is deposited, in (b) is the thickness varying from really thick to less than a monolayer.